Numerical Heat Transfer- Part A: Applications

https://www.tandfonline.com/toc/unht20/current

Accepted November 10th 2023

ELECTROMAGNETOHYDRODYNAMIC (EMHD) CONVECTIVE TRANSPORT OF A REACTIVE DISSIPATIVE CARREAU FLUID WITH THERMAL IGNITION IN A NON-DARCIAN VERTICAL DUCT

Muhammad Mubashir Bhatti [a,*], O. Anwar Bég [b] and S. Kuharat[b]

[a] College of Mathematics and Systems Science, Shandong University of Science and Technology, Qingdao 266590, Shandong, China

[b] Multi-Physical Engineering Sciences Group, Aeronautical and Mechanical Engineering Department, Corrosion/Coatings Lab, 3-08, SEE Bldg, University of Salford, Manchester, M5W4T, UK.

*Corresponding author- E-mail: mmbhatti@sdust.edu.cn; mubashirme@yahoo.com

ABSTRACT: Reactive electro-conductive non-Newtonian (gel) duct flows arise in a variety of industrial applications including hybrid propulsion, smart rheological manufacturing systems, complex geothermal systems and chemical process engineering. Motivated by these technological applications, a mathematical model is developed to simulate the steady, laminar exothermic reactive electro-magneto-hydrodynamic combustible non-Newtonian natural convective transport in a vertical duct. Static uniform axial electrical field and transverse magnetic field are imposed. The Frank-Kamenetskii thermal explosion theory is utilized and also the Carreau fluid model, the latter due to its ability to simulate shear-thinning, Newtonian and shear-thickening behaviour. The duct contains a homogenous, isotropic porous medium and to accomodate Forchheimer inertial drag effects, a non-Darcian model is deployed. The duct walls are permeable enabling suction and injection effects to be studied. Viscous and Joule heating (Ohmic dissipation) are also featured in the model. Following a scaling transformation, the dimensionless emerging non-linear ordinary differential boundary value problem is solved with a robust numerical method (Mathematica shooting algorithm). Validation with an Adomian decomposition method (ADM) is included. Velocity, temperature, duct wall skin friction and Nusselt number are computed for the influence of all key parameters and depicted in graphs and tables. Detailed physical interpretations are provided and some pathways for future investigations are briefly outlined.

KEYWORDS: *EMHD gel propellants; F-K thermal explosion theory; Darcy-Brinkman-Forchheimer porous medium; Carreau non-Newtonian fluid; Numerical simulation.*

1. INTRODUCTION

Heat transmission and thermal ignition in porous media feature in an extensive range of applications spanning geological and chemical energy storage (i.e., packed beds), environmental engineering (i.e., groundwater flow and soil remediation), building materials (i.e., design and optimization of construction industry insulation materials), chemical process engineering (i.e., catalysis, filtration, and adsorption) and propulsion (i.e., hybrid rheological gel propellants, detonation-based propulsion etc) [1-5]. The major breakthrough in thermal explosion (ignition) theory was made by Russian scientist, Frank-Kamenetskii [6] who generalized the earlier Semenov model [7] (which assumed a linear model for the heat conduction process instead of the Laplacian operator). F-K model provides a good framework for simulating thermal explosions of a homogeneous mixture of reactants, under isothermal boundary conditions. It deploys Arrhenius chemical kinetics and intrinsic to this approach is that during the early stages of ignition, negligible reaction consumption occurs. Based on a single step global reaction, only the energy equation is modified to include an exponential term embodying the quantity of heat released per unit mas of fuel consumption. In modern propulsion systems e.g. automotive and aerospace, the catalytic converter is made up of precisely separated platinum-iridium catalyst (creating a porous matrix) that serves as a platform for exothermic chemical processes in which unburned hydrocarbons entirely combust. This helps to reduce hazardous automobile pollutants, such as carbon monoxide, from entering the environment. As a result, the thermal criticality of a burner based on combustion by means of a porous material, such as a catalytic converter, must be researched in order to stabilize, ignite, and drive under steady-state circumstances. Mathematical models of heat transmission and thermal ignition via porous media initiate a non-linear diffusion problem, and the long-term behavior provides useful insight into the intrinsically complicated physical mechanism of thermal runaway in the system. Moreover, in certain reactive flows, variations in fluid density induce natural convection, which arises from the exothermic heat release of a reaction, subsequently influencing the

reaction rate. The intricate interplay between convection and reaction is often regarded as a significant contributing element to the many instabilities found in these flows characterized by chemical reactions. In certain instances, such as the containment of self-igniting substances, these non-homogeneous flows are hypothesized to play a role in impeding (or prolonging) thermal explosions. Conversely, in other scenarios, such as a reaction occurring within a densely packed container, these non-homogeneous flows may result in the creation of localized areas of high temperature, which should be mitigated. The progression of an exothermic chemical reaction may be significantly impacted by the influence of natural convection. Chemical vapor deposition systems, the synthesis of ceramic materials through self-propagating reactions, tubular laboratory reactors, geochemical processes in reservoirs, and the oxidation of solid materials in large containers are a few notable instances that exemplify the interplay between chemical reactions and free convection flows. In recent years, many investigations have been conducted using the Frank-Kamenetskii thermal explosion model. Law and Law [8] used matched asymptotic expansions to calculate the igniting process in a constant laminar boundary-layer flow of a combustible mixture across a hot, isothermal, non-permeable, non-catalytic flat plate with a significant activation energy. In their study, Li et al. [9] developed a locally comparable solution to analyze the thermal ignition of a reactive boundary-layer flow over a heated wedge/cone surface. In their study, Bég et al. [10] used a multi-step differential transform approach and Padé approximants to model the thermal ignition in a combusting flow originating from a slanted slope, which serves as a representation of the spread of forest fires. The researchers conducted a comprehensive analysis of the influence of the Frank-Kamenetskii parameter on the thermal buoyancy effects. Additional investigations of the Frank-Kamenetskii theory have been conducted by Martínez-Ruiz et al. [11] in the field of flame spray dynamics, as well as by Bég et al. [12] in the realm of elastico-viscous hypergolic bi-propellant rocket fuel conduction-convection, specifically examining various Biot numbers. The Frank–Kamenetskii theory has also been deployed in porous media simulation using Darcy, Darcy-Forchheimer and Darcy-

Brinkman models. In their study, Hashmi et al. [13] used homotopy solutions to analyze the impact of heat source/sink effects on mixed convection in the flow of an axisymmetric hydromagnetic viscoelastic Oldroyd-B fluid between two infinite isothermal stretching disks. The heat and momentum characteristics were calculated for a broad spectrum of Frank-Kamenetskii parameter values. In a scholarly manner, Gordon [14] conducted a comprehensive analytical investigation on the phenomenon of thermal explosion occurring inside Darcy porous medium. Thermal ignition in natural convection inside porous media saturated with nanofluids has also been investigated by many researchers. In their study, Rahman et al. [15] used a Galerkin weighted residual finite element approach to analyze the characteristics of natural magneto-convection flow inside an inclined nanofluid saturated porous square cavity. The investigation also included the presence of a Frank-Kamenstkii exothermic chemical reaction and Arrhenius kinetics. The authors observed that the convective patterns are significantly affected by both the Rayleigh and Frank-Kamenetskii numbers. They found that the average Nusselt number is increased when the Frank-Kamenetskii parameter (indicating a more exothermic response) is higher, while it is decreased with higher Rayleigh numbers. Further investigations include Makinde [16] who studied exothermic explosions in a slab using the series summation approach. Salawu et al. [17] addressed an identical problem utilizing the Oldroyd 8-constant fluid model and the weighted residual approach to resolve the nonlinear formulation. Adesanya et al. [18] generalized these studies [16, 17] to consider entropy generation minimization in thermal ignition of third grade Reiner-Rivlin gel propellants in a horizontal duct with wall Biot number effects. They noted that entroby generation rate is elevated with Frank-Kamenetskii parameter (since exothermic chemical interactions amplify the heat transfer rate from the combustion zone to the cool wall) whereas it is suppressed with increment in third grade material (non-Newtonian) parameter.

The above studies did not consider electrohydrodynamics (EHD) or magnetohydrodynamics (MHD) effects. In recent years, new electroconductive rheological propellants have emerged, in for example, space propulsion which contain

metallic particles and achieve greater burn efficiency than conventional fuels [19-22]. These complex liquids exhibit both rheological [23] and electromagnetic properties-the latter enables their manipulation with external electrical and/or magnetic fields. These complex liquids can be deployed in electrothermal, electrostatic or magneto-static thrusters [19] and may also be utilized with lasers to boost combustion characteristics. The non-Newtonian characteristics of these electromagnetic gel fuels have been determined experimentally to range from shear thinning to shear thickening [24-27]. Accurate simulation of the fluid dynamics of these gels therefore can be achieved with appropriate rheological models, including Cross, power-law and in particular the Carreau model [28]. The latter has been originally developed for polymer dynamics and later applied to blood and other complex suspensions. It is a generalization of simpler power-law models featuring five parameters, namely a zero-shear viscosity, infinite shear viscosity, time constant, transition parameter, and power law exponent. An advantage of this model is the clearly delineated upper (zero shear viscosity) and lower (infinite shear viscosity) limits for the polymer viscosity. To simulate the dynamics of electromagnetic non-Newtonian gels in combustion systems, a generalized formulation is required featuring electrical body force, magnetohydrodynamic body force, modified viscosity (rheology) and thermal explosion based on Arrhenius kinetics [29]. While a number of studies have examined magnetohydrodynamic rheological duct and boundary layer flows, thus far electrohydrodynamic non-Newtonian duct flows have not been explored using the Frank-Kamenetskii exothermic reaction model. Salawu and Okedoye [30] conducted a thermodynamic optimization study of two-step exothermic chemically reacting hydromagnetic flow with heat transfer in a channel using the second law of thermodynamics. The entropy generation rates in a duct flow of couple stress fluid with hydrodynamic slip effects at the wall were estimated by Salawu et al. [31]. In their study, Makinde and Bég [32] used a perturbation method combined with a modified Hermite-Padé approximation technique to evaluate the volumetric generation of entropy and thermal stability in a reactive magnetohydrodynamic isothermal duct flow. The researchers conducted an analysis to ascertain the velocity,

temperature distribution, and thermal criticality conditions associated with the influence of the Frank-Kamenetskii parameter.

Another major development in recent years has been the deployment of porous media in combustion systems. A popular porous medium deployed in for example rocket fuel injectors is *Rigimesh* which is a relatively dense, non-uniform, fibrous porous medium. This provides an excellent control mechanism in both duct flows and injector plates in liquid-based rocket combustion [33-36]. The established approach in simulating hydrodynamics of porous media is the Darcy model, which assumes laminar flow in the formation and assumes a linear relationship between flow rate and pressure drop. At higher velocities, as encountered in propulsion systems, inertial effects become prominent. The flow departs from the classical Darcy model and non-Darcy effects emerge [37, 38]. Motivated by both rocket duct and other e. g. chemical engineering processing applications, a number of ivestigators have studied theoretically Newtonian or non-Newtonian and electro/magnetc fluid dynamic transport in ducts containing either Darcian or non-Darcy porous media. Frequently used non-Darcy formulations include the Darcy-Brinkman model (which accounts for vorticity diffusion), Darcy-Forchheimer model and the combined Darcy-Brinkman-Forchheimer drag force model. These approaches are based on a volume averaging of porous medium effects and ignore tortuosity and anisotropy of the medium. Bég and Makinde [39] used MATLAB to compute the mass transfer and flow in a Maxwell viscoelastic fluid saturated porous medium duct with Darcy's model. Umavathi and Bég [40] obtained perturbation solutions for homogenous reactions in thermo-solutal transport in anon-Darcy porous medium upright duct with asymmetric convective wall boundary conditions, noting the strong deceleration induced at higher Forchheimer numbers. The Darcy-Forchheimer formulation has also been implemented recently in hydromagnetic non-Newtonian flows in porous media. Nasir et al. [41] deployed Liao's HAM approach to derive higher-order (up to 30) power series solutions for non-Fourier, non-Fickian electroconductive Reiner–Rivlin second-grade rheological nanofluid flow in Darcy-Forchheimer porous media under a transverse magnetic field. Rawat et al. [42] used a variational finite element method

(FEM) to simulate the unsteady hydromagnetic buoyancy-driven thermo-solutal convection in a geothermal duct with heat generation and thermal conductivity variation effects. Geindreau and Aurialut [43] conducted a rigorous analysis of creeping magnetohydrodynamic (MHD) transport in a Darcian porous medium. They used upscaling at the pore level to derive the magnetic version of the Darcy seepage law with macroscopic magnetic field and electric flux. They used asymptotic expansions to show that there is a strong coupling of the macroscopic mass flow and electric current and that both are influenced by the macroscopic pressure gradient in addition to the electric field. They also showed that Hartmann magnetic number strongly modifies the permeability tensor. Further investigations of MHD flows in porous media with heat and mass transfer include McWhirter et al. [44] (experimental works in fusion propulsion systems), Yih [45] (transpiring stagnation flow boundary layers), Ghosh et al. [46] (unsteady spinning of magnetic Stokesian polar liquids), Zueco et al. [47] (Hall magneto-gas dynamic accelerator flows deploying non-Darcy duct designs) and Maqbool et al. [48] (revolving and oscillating duct fractional viscoelastic MHD flows).

Significantly less work has been reported in electrohydrodynamic (EHD) flows in purely fluid regimes or porous media ducts [49]. Different formulations are available for electrofluid dynamics and can feature either electrical body forces, electro-osmotic body forces and ion diffusion and other electrical field phenomena. Narla et al. [50] presented a novel model for electrokinetic insect respiratory-inspired microfluidic membrane pumping by solving the Poisson–Boltzmann electrical potential equation. They noted that axial electrical field has different effects depending on its orientation. In the aligned case, wall shear stress is reduced whereas in the reverse orientation case it is boosted. They also showed that volumetric flow rate and wall shear stress are both elevated with a reduction in electrical double layer (EDL) thickness. Bég et al. [51] studied EHD ion drag duct pumping dynamics in aerospace flow control using spectral codes. They computed the impact of electrical Hartmann number, electrical Reynolds number, electrical slip and source parameters on electrical field, potential and charge density distributions. Tripathi et al. [52] derived analytical solutions for

electrokinetic polar (couple stress) peristaltic propulsion in a microchannel. Bedolla et al. [53] evaluated the corona-discharge-induced electrohydrodynamic flow in a high-voltage asymmetric capacitor duct system with reference to electrostatic space propulsion. Bég et al. [54] derived analytical solutions for fluctuating dielectric hydrogen gas transport in a duct using Adomian decomposition and homotopy methods. They considered both static and alternating electrical and magnetic fields in addition to Maxwell displacement current effects. Further studies include Granados et al. [55] (electrostatic thrusters) and Bouef et al. [56] (on high strength electrical fields in plasma thrusters). All these investigations confirmed that in multiple situations, judicious use of electrical fields can achieve significant benefits in efficiency and flow control. Several researchers have also studied electrohydrodynamic flows in porous media, notably del Río & Whitaker [57] and Auriault and Strzelecki [58]. However, their formulations are very heavily focused on tensorial analysis and yield limited results of value in engineering analysis. An alternative approach has been developed in recent years which focuses on the dominant effects of magnetic body force (Lorentz) and the Gaussian electrical body force within the framework of engineering fluid dynamics. Bhatti et al. [59] studied the collective effects of axial electrical field and transverse magnetic field on peristaltic propulsion in a two-dimensional deformable duct containing a two-phase viscoelastic fluid with radiative flux effects. They showed analytically that temperatures are reduced with higher particle volume fraction and also the pumping rate in retrograde pumping region whereas the contrary response is induced in the co-pumping region. They also found that an elevation in magnetic field intensity i. e. greater Hartmann number depletes the magnitude of the trapping bolus but not the quantity. Vargas et al. [60] studied the influence of variable zeta potential on Taylor dispersion in EMHD microchannel transport. Further studies include Jian and Chang [61] and Si and Jian [62] who respectively considered variable magnetic fields and Jeffreys viscoelastic models.

An inspection of the literature on electromagnetic gel propellant and chemical gel duct flows has revealed that thus far *the influence of Joule and viscous dissipation on*

thermal ignition in a reactive Carreau electro-magneto-hydrodynamic transport with non-Darcy effects has not been addressed. Previous studies have ignored thermal explosions (Frank-Kamenetskii reactions) and either considered electrohydrodynamics with Joule heating alone [62], considered both Joule and viscous heating but neglected non-Newtonian and porous medium effects [63], utlized alternate non-Newtonian models e.g. Williamson viscoelastic model [64] and Bingham viscoplastic model [65] or included viscous heating but neglected Joule heating, non-Darcy and non-Newtonian effects [66]. *The present work therefore significantly generalizes previous studies by considering non-Darcy drag force, wall suction/injection, Carreau rheological model [67, 68], Joule and viscous heating, thermal explosion (Arrhenius kinetics), orthogonal electrical and magnetic fields and thermal buoyancy (natural convection) simultaneously.* A modified formulation for both porous media Darcian and Forchheimer drag forces is deployed in which the effects are also included in the energy conservation equation (quadratic Darcy and cubic inertial drag). The normalized ordinary differential boundary value problem is solved using a robust shooting technique with numerical quadrature. Validation with previous studies and additionally a finite element method (FEM) is included. Graphical and tabulated distributions for axial velocity, temperature, skin friction and Nusselt number are presented for the effects of all key emerging parameters. The current study, while limited to laminar flow, provides a solid theoretical benchmark for future extensions to 3-D flows with computational fluid dynamics (CFD) and turbulence aspects.

2. MATHEMATICAL FORMULATION

Let us assume a fully developed flow of an electro-magneto-hydrodynamic Carreau rheological fluid (gel propellant) propagating through a vertical duct (channel) comprising parallel plates located at a finite distance apart. The duct contains a two-dimensional isotropic porous medium with constant permeability which is saturated with the EMHD Carreau fluid. Both walls of the duct are stationary relative to the fluid motion. The Darcy-Brinkman-Forchheimer model is used to simulate drag force

effects in the permeable medium. Furthermore, an exothermic-reaction is assumed and Frank-Kamenetskii chemical kinetics considered. A Cartesian coordinate system is deployed with the $\underline{y}$ −axis located in the vertical direction and the $\underline{x}$ −axis orientated perpencular to this, in the direction of the flow. Both duct walls are separated by a distance $\underline{h}$.

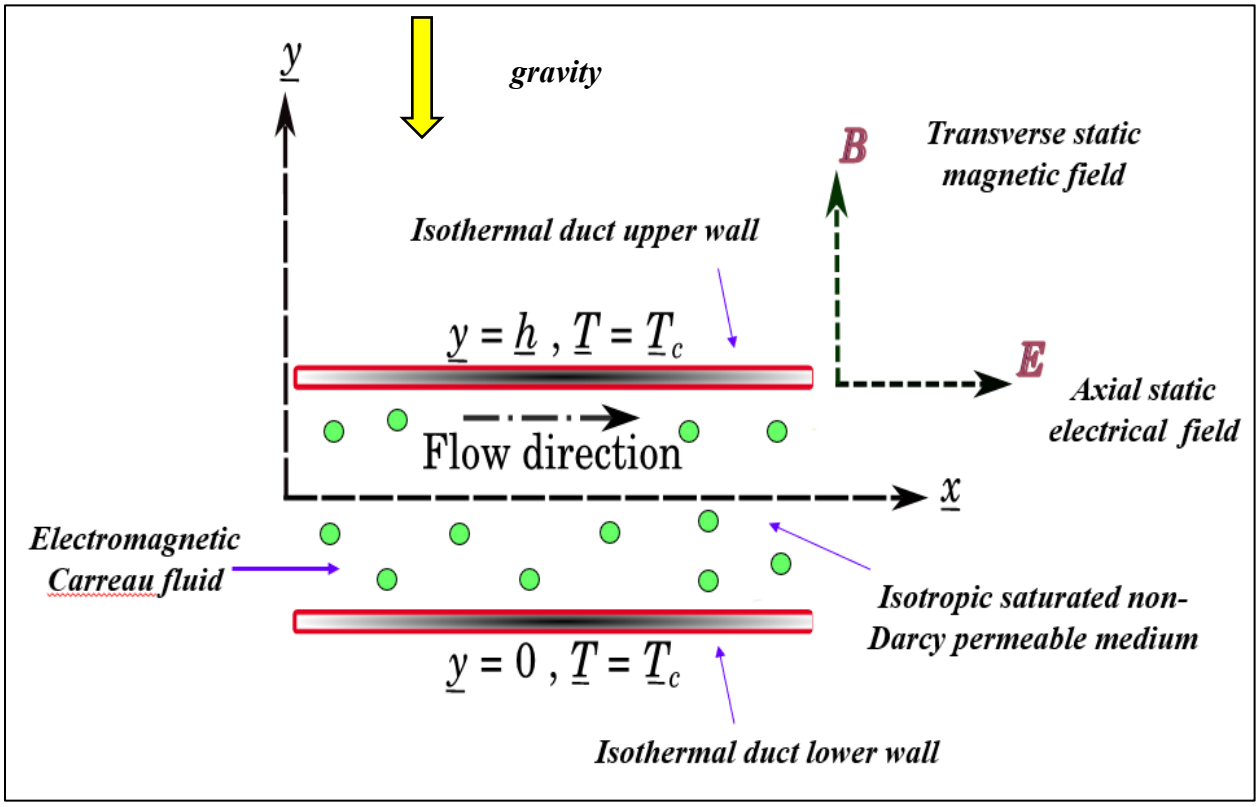

Figure 1: Geometrical model for non-Newtonian thermal explosive EMHD duct flow.

Fig. 1 illustrates the physical model. At the lower duct wall (plate) $\underline{y} = 0$, fluid injection occurs with a uniform rate v_0, and is matched with a corresponding suction of the fluid at the upper duct $\underline{y} = \underline{h}$. Both of the duct walls are held at a constant temperature $\underline{T_c}$. A uniform static external vertical magnetic and orthogonal axial electric field is applied, while the induced magnetic field is ignored. **Fig. 2** summarizes the many components of multi-physics featured in the present fluid dynamics formulation.

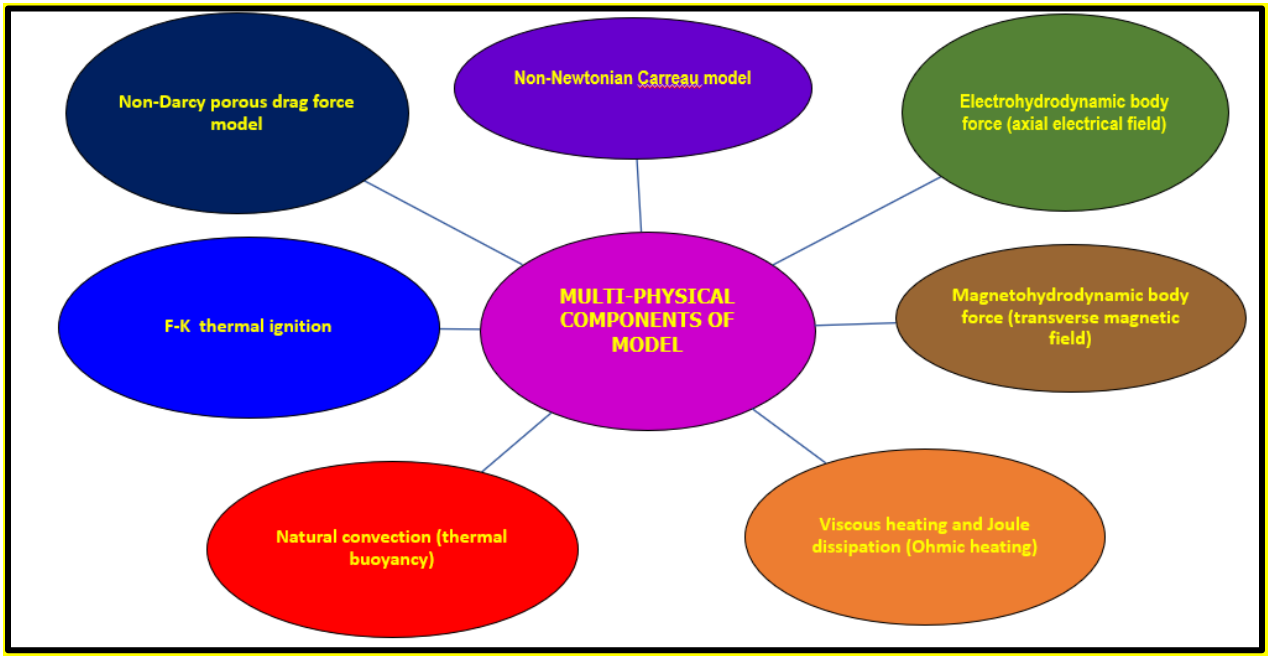

Figure 2: Multi-physical aspects of the present model

2.1 Hydrodynamic equations

The governing mass and momentum conservation equations in view of Ohm's law and the Darcy-Brinkman-Forchheimer model can be written in vectorial form (neglecting magnetic induction, Maxwell displacement and Hall current effects) as:

$$\nabla \cdot \mathbf{U} = 0, \tag{1}$$

$$\rho \frac{d\mathbf{U}}{dt} = \nabla \cdot \underline{p} - \nabla \mathcal{C} - \underline{J} \times \underline{B} + \mathcal{R} + \rho \mathbf{g} \underline{\beta} \left(\underline{T} - \underline{T_c} \right), \tag{2}$$

Here $\mathbf{U}\left(= [u(\underline{y}),0,0]\right)$ denotes the velocity field, ρ indicates the density, $\underline{p}$ the pressure, $\underline{J}\left[= \sigma\left(\mathbf{U} \times \underline{B} + E\right)\right]$ the current density [62], σ the electrical conductivity, E the electric field, $\underline{B}$ the magnetic field, $\mathcal{R}$ the composite body force term for Darcy and Forchheimer drag, $\underline{\beta}$ the thermal expansion coefficient, g gravity. $\mathcal{C}$ denotes the stress tensor of the Carreau fluid model (originally derived using molecular network theory) which may be defined [68] as:

$$\mathcal{C} = \mu(\dot{\xi})\mathcal{A}_1,$$

(3)

where $\mu(\dot{\xi})$ indicates the apparent viscosity and $\mathcal{A}_1$ represents the first Rivlin-Ericksen tensor. They are defined as:

$$\mu(\dot{\xi}) = \mu_{\text{inf}} + (\mu - \mu_{\text{inf}})\left[1 + (\Gamma\dot{\xi})^2\right]^{\frac{n-1}{2}}, \dot{\xi} = \sqrt{2\text{tr}(\mathcal{D}^2)}, \mathcal{D} = \frac{1}{2}(\nabla\mathbf{U} + (\nabla\mathbf{U})^t) = \frac{1}{2}\mathcal{A}_1,$$

(4)

The Carreau model is a five-parameter rheological model in which μ denotes the viscosity associated with zero shear rate and μ_{inf} the viscosity associated with infinite shear rate, Γ the time constant, $\dot{\xi}$ the strain rate tensor and n the power-law (rheological) index. The fluid exibits shear-thinning (pseudoplasticity) behavior when $0 < n < 1$, Newtonian behavior for $n = 1$ and shear-thickening (dilatancy) for $n > 1$. Carreau fluid exhibits Newtonian behavior at low shear rates and transforms into a power-law fluid at high shear rates. We adopt the assumption that viscosity at an infinite shear rate is zero in the suggested mathematical formulation. Therefore:

$$\mu(\dot{\xi}) = \mu\left[1 + (\Gamma\dot{\xi})^2\right]^{\frac{n-1}{2}}.$$

(5)

The porous medium drag force $\mathcal{R}$ comprises contributions from a *linear Darcy drag term* and a *quadratic inertial Forchheimer term*, and may be written as [**64**]:

$$\mathcal{R} = -\frac{\mu(\dot{\xi})}{k}\mathbf{U} - \frac{\rho C_f}{\sqrt{k}}|\mathbf{U}|\mathbf{U}, \quad (6)$$

where k is the isotropic permeability of the porous medium and C_f represents the Forchheimer coefficient.

2.2 Heat transfer

The energy equation incorporating the effects of Joule heating and viscous dissipation assuming the classical Fourier heat conduction law, can be stated as [63, 81-82] :

$$\rho C_p \frac{dT}{dt} = \mathcal{C}: gradU - \nabla\mathcal{H} + \frac{\underline{J}\cdot\underline{J}}{\sigma} - \mathcal{R} + \mathcal{Q}\mathcal{S}\mathcal{K},$$

(7)

Here C_p indicates the specific heat, $\mathcal{H}(=-\kappa\nabla T)$ is the Fourier heat flux vector, κ the thermal conductivity, Q the heat of reaction term, $\mathcal{S}$ the reactant species, and $\mathcal{K}$ is the temperature dependent reaction rate which is described by [**69**]:

$$\mathcal{K} = \mathcal{A}\left(\frac{\overline{K}\underline{T}}{\nu\mathcal{L}}\right)^{m} \exp\left(-\frac{\overline{E}}{\overline{R}\underline{T}}\right),$$

(8)

Here the exponent $m \in (-2; 0; 0.5)$, which indicates the chemical kinetics for sensitized, Arrhenius and bimolecular reactions, and $\mathcal{A}$ is the m^{th} order rate constant for chain branching, $\overline{K}$ represents the Boltzmann's constant, ν represents the vibration frequency, $\mathcal{L}$ is Planck's number, $\overline{E}$ is activation energy, and $\overline{R}$ the gas constant.

The momentum and energy equations can be shown to assume the following forms in light of the aforementioned equations and presumptions:

$$v_0\rho\frac{du}{d\underline{y}} = -\frac{d\underline{p}}{d\underline{x}} + \frac{d}{d\underline{y}}\left(\mu\left[1+\left(\Gamma\frac{du}{d\underline{y}}\right)^2\right]^{\frac{n-1}{2}}\frac{du}{d\underline{y}}\right) - \sigma B_0^2 u + \sigma B_0 E - \left[1+\left(\Gamma\frac{du}{d\underline{y}}\right)^2\right]^{\frac{n-1}{2}}\frac{\mu}{k}u$$
$$-\frac{C_f\rho}{k^{1/2}}u^2 + g\rho\underline{\beta}(\underline{T}-\underline{T_c}),$$

(9)

$$v_0\rho C_p\frac{d\underline{T}}{d\underline{y}} = k\frac{d^2\underline{T}}{d\underline{y}^2} + \mu\left[1+\left(\Gamma\frac{du}{d\underline{y}}\right)^2\right]^{\frac{n-1}{2}}\left(\frac{du}{d\underline{y}}\right)^2 + \sigma B_0^2 u^2 + \sigma E^2 - 2\sigma E B_0 u$$
$$+\left[1+\left(\Gamma\frac{du}{d\underline{y}}\right)^2\right]^{\frac{n-1}{2}}\frac{\mu}{k}u^2 + \frac{C_f\rho}{k^{1/2}}u^3 + Q\mathcal{S}\mathcal{A}\left(\frac{\overline{K}\underline{T}}{\nu\mathcal{L}}\right)^{m}\exp\left(-\frac{\overline{E}}{\overline{R}\underline{T}}\right).$$

(10)

The boundary conditions at the left and right duct walls are prescribed as:

$$u = 0, \qquad \underline{T} = \underline{T_c}, \qquad \underline{y} = 0, \tag{11}$$

$$u = 0, \qquad \underline{T} = \underline{T_c}, \qquad \underline{y} = \underline{h}. \tag{12}$$

In the framework of the mathematical modeling, the following dimensionless variables are invoked:

$$u = \frac{u}{\underline{v_0}}, y = \frac{\underline{y}}{\underline{h}}, T = \frac{(\underline{T} - \underline{T_c})\overline{E}}{\underline{T_c^2}\overline{R}}. \tag{13}$$

Here *u is non-dimensional axial velocity, y is scaled transverse coordinate and T is dimensionless temperature*. Utilizing eqn. (13) in eqns. (11), (12), leads to the following form of the coupled, nonlinear dimensionless ordinary differential equations for monetum and heat (energy):

$$\alpha\frac{du}{dy} = P + \left[1 + \left(We\frac{du}{dy}\right)^2\right]^{\frac{n-1}{2}}\frac{d^2u}{dy^2} + (n-1)\left(We\frac{du}{dy}\right)^2\left[1 + \left(We\frac{du}{dy}\right)^2\right]^{\frac{n-3}{2}}\frac{d^2u}{dy^2} - H_a^2u + E_l - \left[1 + \left(We\frac{du}{dy}\right)^2\right]^{\frac{n-1}{2}}D_au - D_fu^2 + G\theta, \tag{14}$$

$$\alpha\mathrm{Pr}\frac{dT}{dy} = \frac{d^2T}{dy^2} + \xi_1\left[1 + \left(We\frac{du}{dy}\right)^2\right]^{\frac{n-1}{2}}\left(\frac{du}{dy}\right)^2 + \xi_1H_a^2u^2 - \xi_2u + \xi_3 + \left[1 + \left(We\frac{du}{dy}\right)^2\right]^{\frac{n-1}{2}}\xi_1D_au^2 + \xi_1D_fu^3 + \lambda(1+\beta_r\theta)^m\exp\left(\frac{\theta}{1+\beta_r\theta}\right), \tag{15}$$

Here the following dimensionless parameters are featured: α represents the wall injection/suction, We the Weissenberg number (ratio of elastic to viscous forces), H_a the Hartmann number (ratio of Lorentz magnetic to viscous forces), E_l the electric field parameter (ratio of modified electrical body force to viscous force), D_a the Darcy

number (dimensionless permeability parameter), D_f the Forchheimer number (dimensionless inertial drag force parameter), P the dimensionless pressure gradient parameter, G the thermal Grashof number (ratio of thermal buoyancy to viscous forces), β_r the activation energy parameter, ξ_1 the Brinkman (viscous dissipation) number, ξ_2 is heat generation parameter expressing the relative contribution of the interaction of magnetic and electric fields to heat conduction in the regime, ξ_3 represents the Joule heating (Ohmic dissipation) parameter, Pr is the Prandtl number and λ is the Frank-Kamenetskii parameter [**5**]. These parameters are all defined as follows:

$$\alpha = \frac{v_0 \underline{h}}{\mu}, We = \frac{\Gamma v_0}{\underline{h}}, H_a^2 = \frac{\sigma \underline{h}^2 B_0^2}{\mu}, E_l = \frac{\sigma B_0 E \underline{h}^2}{\mu v_0}, D_a = \frac{\underline{h}^2}{k}, D_f = \frac{C_f v_0 \underline{h}^2}{\nu\sqrt{k}}, P = -\frac{\underline{h}^2}{\mu v_0}\frac{dp}{d\underline{x}}, G = \frac{g\beta \underline{h}^2 \underline{T_c} \beta_r}{\nu v_0}, \beta_r = \frac{\overline{R}\underline{T_c}}{\overline{E}}, \xi_1 = \frac{\mu v_0^2}{\kappa \underline{T_c} \beta_r}, \xi_2 = \frac{2\sigma B_0 E v_0 \underline{h}^2}{\underline{T_c} \kappa \beta_r}, \xi_3 = \frac{\sigma E^2 \underline{h}^2}{\underline{T_c} \kappa \beta_r}, \Pr = \frac{\mu C_p}{\kappa},$$
$$\lambda = \frac{\mathcal{Q}\mathcal{S}\mathcal{A}\overline{E}\underline{h}^2 \overline{K}^n \underline{T_c}^n \exp\left(-\frac{1}{\beta_r}\right)}{\nu^n \mathcal{L}^n \underline{T_c}^2 \overline{R} \kappa}. \tag{16}$$

The boundary conditions may be expressed in a dimensionless form as follows:

$$u = 0, \qquad T = 0, \qquad y = 0, \tag{17}$$

$$u = 0, \qquad T = 0, \qquad y = 1. \tag{18}$$

The dimensionless wall shear stress (coefficient of skin friction) and Nusselt number and the can be expressed using the following definitions:

$$S_f = \frac{du}{dy}\left[1 + \left(We\frac{du}{dy}\right)^2\right]^{\frac{n-1}{2}}\Bigg|_{y=0}, \qquad N_u = \frac{dT}{dy}\Big|_{y=0}. \tag{19}$$

3. NUMERICAL SOLUTION AND VALIDATION

Using the shooting technique, we acquired numerical solutions using the symbolic software Mathematica for the boundary value problem defined by Eqns. (14) and (15)

subject to boundary conditions (17) and (18). The NDSOLVE numerical shooting methodology [70] is a versatile and effective technique for solving coupled non-linear differential equations. The technique in problem is designed to model boundary conditions by treating them as a multivariate function that depends on initial conditions at a particular point. Consequently, the boundary value issue is deconstructed into the objective of identifying the beginning circumstances that provide a root. The NSOLVE approach exhibits high efficiency, however with a lower level of accuracy compared to finite difference or collocation methods. Nevertheless, it is worth noting that NDSOLVE has remarkable stability and convergence properties when applied to nonlinear fluid dynamics equation systems that are well-posed [70]. The adaptive approach is used to ascertain the magnitude of the step size. Typically, when the solution exhibits significant fluctuations within a certain location, NDSolve will adjust the step size in order to enhance the accuracy of solution tracking. The NDSolve tool provides the capability to specify the desired precision or accuracy of the results. The method used is shown in **Fig. 3**.

```
{vsol, {data}} = Reap[
    NDSolve[{y1'[t] == y2[t]                    y1[0] == 2
             y2'[t] == 1000 (1 - y1[t]^2) y2[t] - y1[t]  y2[0] == 0},
      {y1, y2}, {t, 3000}, Method → {MonitorMethod,
        "MonitorFunction" → Function[{h, sd, mord},
          Sow[{NDSolve`SolutionDataComponent[sd, "Time"],
            RealExponent[h], mord}]]}]];
Plot[y1[t] /. vsol, {t, 0, 3000}]
```

Fig. 3: NDSOLVE algorithm [**73**]

Validation of the proposed model, which incorporates several physical effects, is accomplished by a comparative analysis with an alternate numerical approach. The Adomian decomposition technique (ADM) has been widely used in many complicated

multi-physical boundary value problems [71]. The ADM involves the decomposition of an unknown function, denoted as $u(x,t)$, which appears in ordinary or partial differential equations. This decomposition is achieved by using a recursive method that separates $u(x,t)$ into a sum of linear and nonlinear components, with a finite number of terms. Efficient assessment of these components may be accomplished by the use of recursive relations that include simple integrals. After the process of decomposition is carried out, the linear operator in the differential equation is inverted, specifically targeting the highest-order derivative operator present on both sides. Subsequently, the starting and/or boundary conditions are discerned as expressions only reliant on the independent variable, serving as an initial approximation. The formulation of the nonlinear function decomposition is expressed in relation to a set of specialized polynomials known as Adomian polynomials. The terms of the series solution are generated using a recurring relation employing Adomian polynomials. Symbolic software MATLAB v 19 was deployed to compute the Adomian polynomials in the in-house code "ADSIM" and monitor convergence of the series of the function. Convergence is excellent with this technique as noted in Cherruault [**72**]. Further details on the construction of Adomian polynomials is given in Bég *et al.* [**73**] and Shamshuddin *et al.* [**74**] and in **Appendix 1.** To execute the numerical procedure in both MATHEMATICA NDSOLVE and in the MATLAB "ADSIM" inhouse code, the following parameter values have been chosen: $D_a = 0.5; H_a = 1; E_l = 1; We = 0.1; D_f = 0.5; \xi_1 = 3; \xi_2 = 0.3; \xi_3 = 0.1; P = 1; G = 3; \alpha = 1; Pr = 3; m = 0.3; \beta_r = 0.1; \lambda = 0.02; n = 3.$ All data is selected to reflect actual electromagnetic gel propellants [62-67]. **Tables 1 and 2** document the comparison of the NDSOLVE and ADSIM semi-numerical solutions. Very close correlation between the two solutions is achieved.

Table 1: Skin friction comparison for NDSOLVE and ADSIM with various parameters

n	D_a	D_f	We	H_a	G	λ	ξ_1	ξ_2	m	β_r	α	S_f (NDSOLVE)	S_f (ADSIM)
0.1												0.801148	0.801201
1												0.801338	0.801357
10												0.803206	0.803197
	0.5											0.801757	0.801743
	1											0.776311	0.776295
	2											0.73076	0.73084
		0.5										0.801757	0.801721
		4										0.772299	0.772283
		7										0.751146	0.751205
			0									0.801338	0.801352
			0.2									0.803002	0.803000
			0.4									0.807631	0.807644
				0								0.858892	0.858879
				0.5								0.843746	0.843756
				1								0.801757	0.801737
					0							0.749741	0.749728
					1							0.765249	0.765256
					2							0.782452	0.782438
						0.3						0.826493	0.826530
						0.4						0.835762	0.835722
						0.5						0.845281	0.845266
							3					0.801757	0.801751
							4					0.82187	0.821863
							5					0.845316	0.845323
								0.1				0.804619	0.804646
								0.3				0.801757	0.801751
								0.5				0.798928	0.798921
									-2			0.801734	0.801743
									0			0.801754	0.801761
									0.5			0.80176	0.801754
										0.1		0.801757	0.801754
										0.3		0.801762	0.801774
										0.5		0.801767	0.801773
											-0.5	1.05082	1.05092
											0	0.972825	0.972794
											0.5	0.887331	0.887353

Table 2: Nusselt number comparison for NDSOLVE and ADSIM with various parameters.

n	D_a	D_f	We	H_a	G	λ	ξ_1	ξ_2	m	β_r	α	N_u (NDSOLVE)	N_u ($ADSIM$)
0.1												0.319313	0.319322
1												0.318696	0.318684
10												0.312945	0.312303
	0.5											0.317353	0.317356
	1											0.303406	0.303421
	2											0.278922	0.278944
		0.5										0.317353	0.317401
		4										0.299557	0.299588
		7										0.28701	0.287022
			0									0.318696	0.318722
			0.2									0.313595	0.313604
			0.4									0.30143	0.301423
				0								0.349329	0.349355
				0.5								0.340769	0.340811
				1								0.317353	0.317394
					0							0.273027	0.273035
					1							0.285839	0.285844
					2							0.300452	0.300491
						0.3						0.42446	0.42452
						0.4						0.464237	0.464265
						0.5						0.504892	0.504932
							3					0.317353	0.317377
							4					0.439708	0.439728
							5					0.580665	0.580661
								0.1				0.327083	0.327076
								0.3				0.317353	0.317381
								0.5				0.307731	0.307744
									-2			0.317274	0.317288
									0			0.317343	0.317421
									0.5			0.31736	0.317451
										0.1		0.317353	0.317449
										0.3		0.317369	0.317501
										0.5		0.317386	0.317403
											-0.5	0.692313	0.692505
											0	0.571681	0.571692
											0.5	0.436304	0.436422

4. GRAPHICAL NDSOLVE SOLUTIONS

Figures 4-22 depict the distributions in velocity, temperature profiles, skin friction, and Nusselt number profiles for all key rheological, thermophsyical, porous media and electromagnetic parameters.

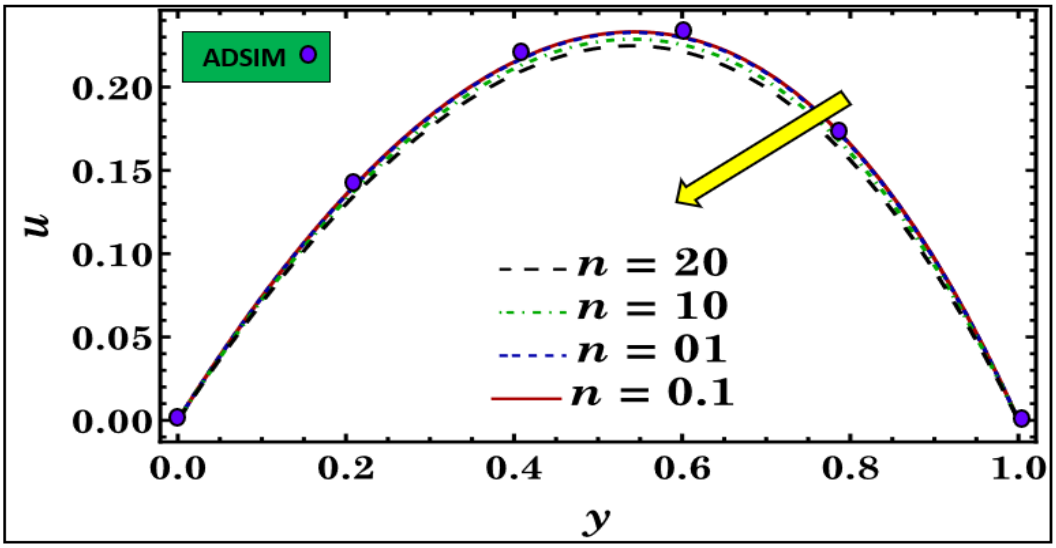

Figure 4: Velocity profile for influence of rheological Carreau power-law index n.

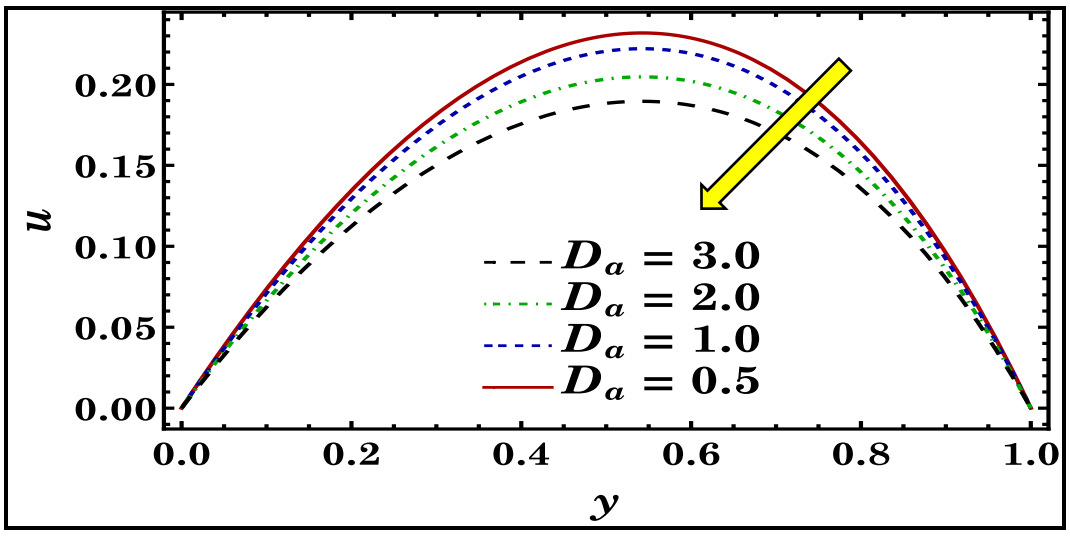

Figure 5: Velocity distribution with influence of Darcy number D_a.

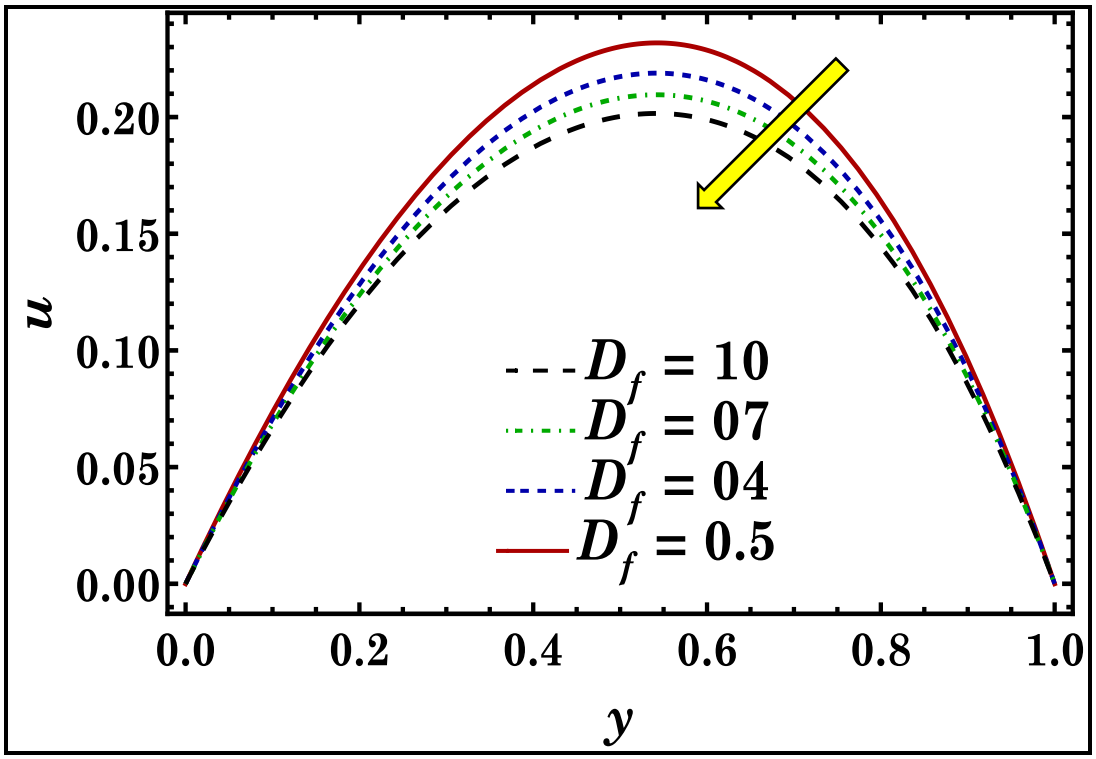

Figure 6: Velocity distribution with variation in Forchheimer number D_f.

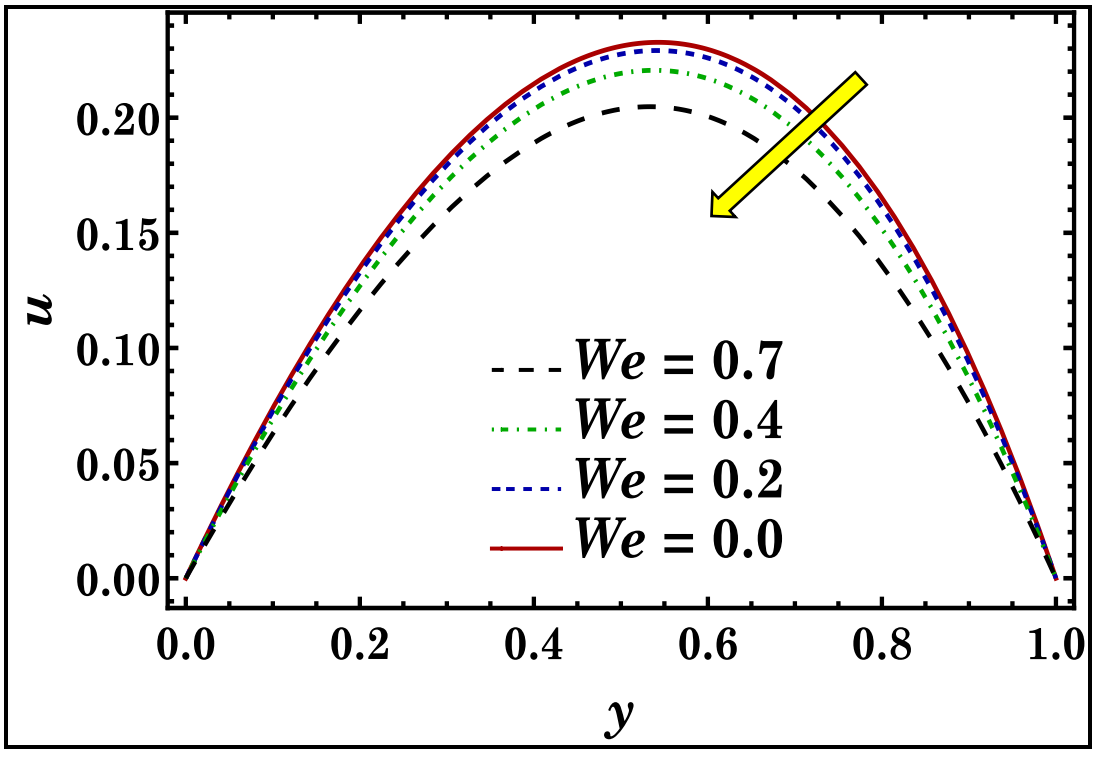

Figure 7: Velocity distribution with influence of Weissenberg number We.

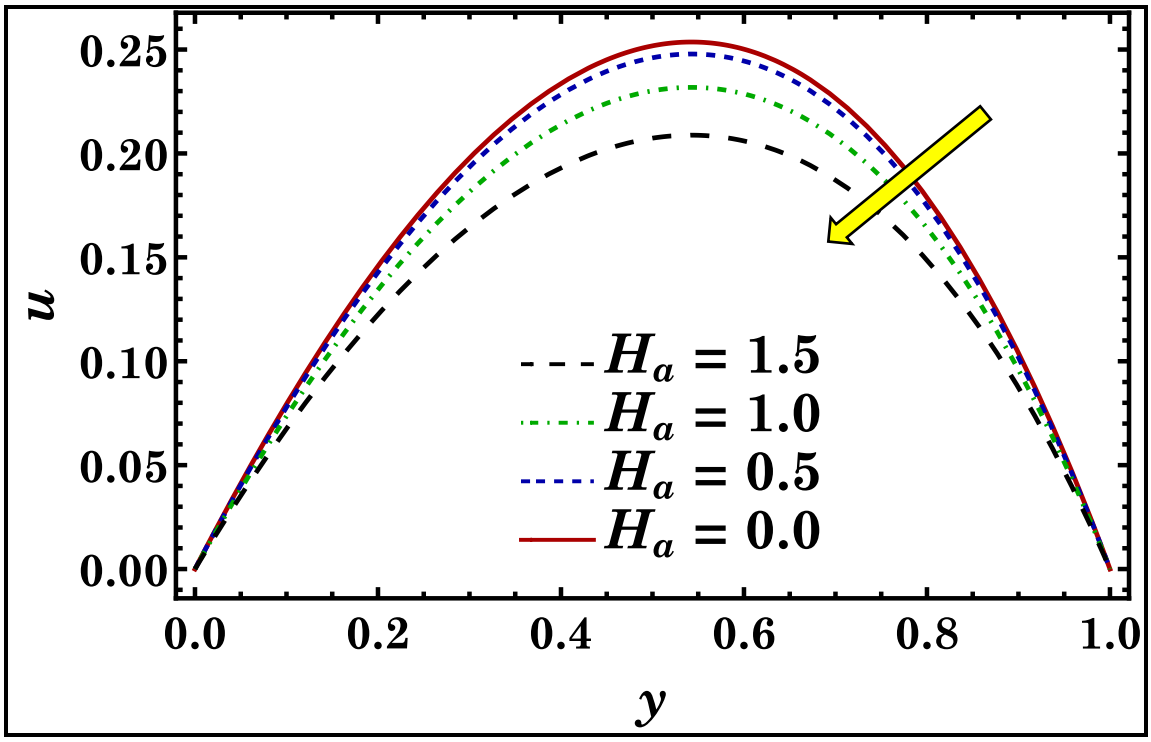

Figure 8: Velocity distribution with influence of Hartmann (magnetic) number H_a.

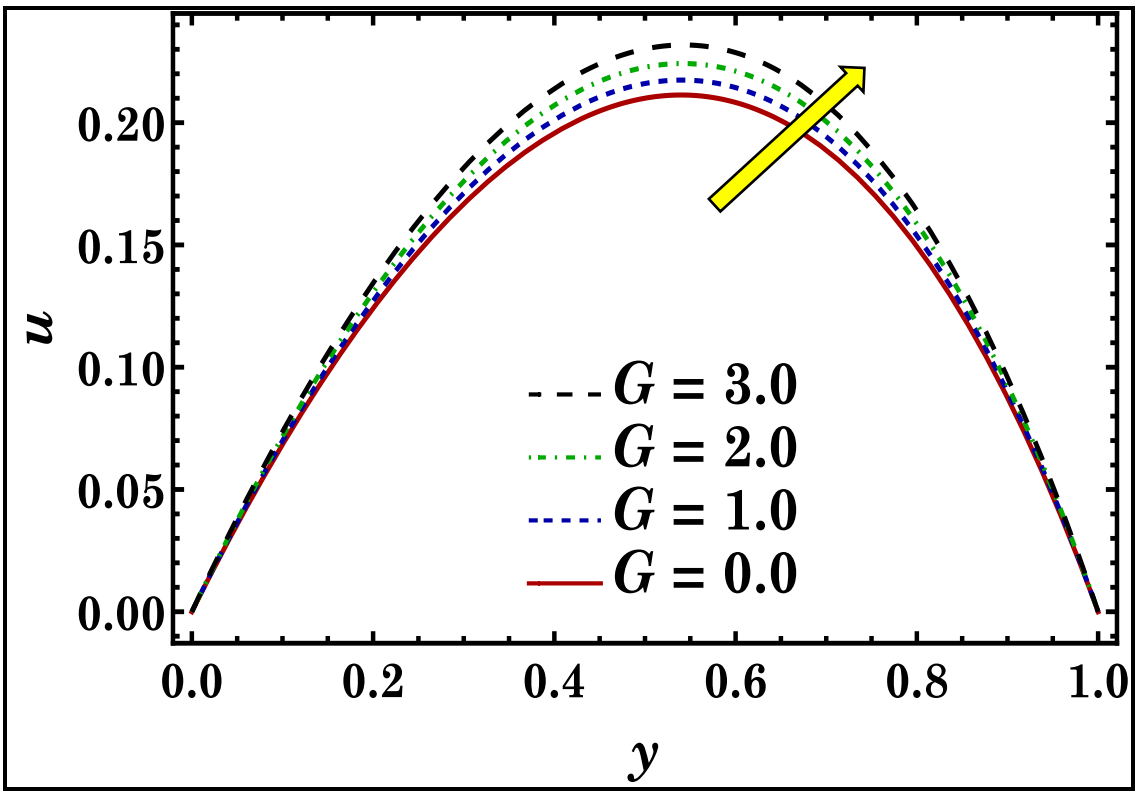

Figure 9: Velocity distribution with influence of Grashof number G.

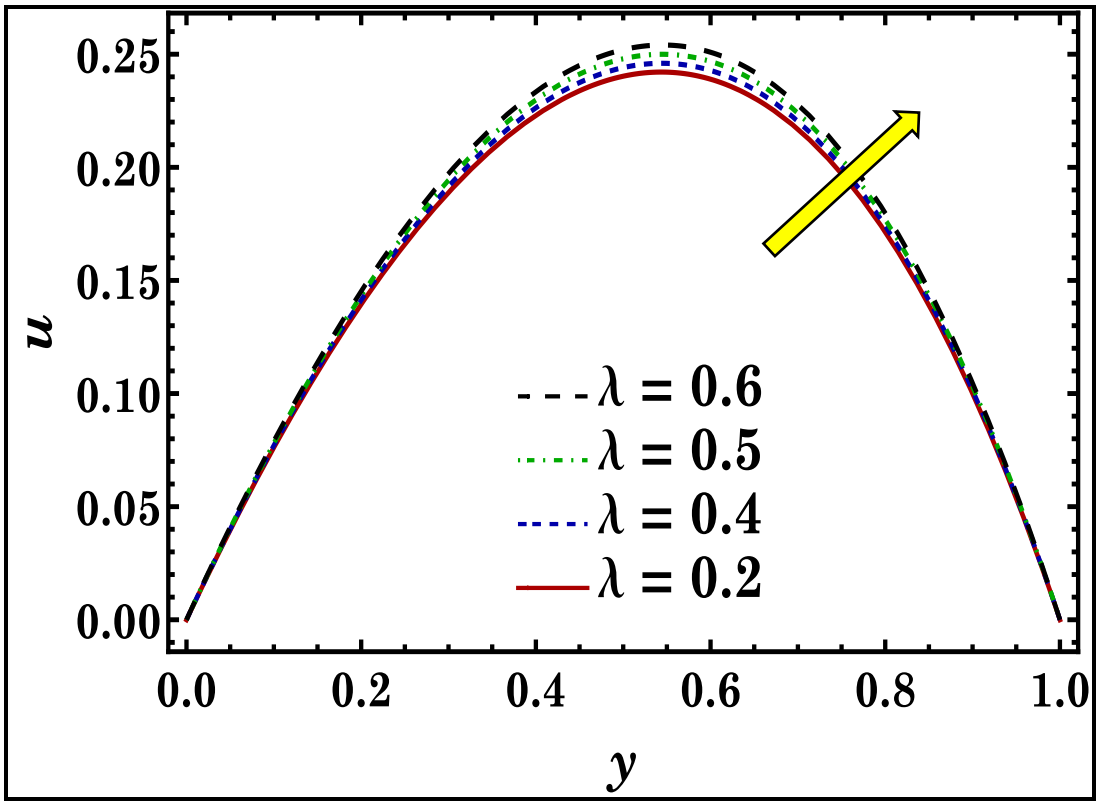

Figure 10: Velocity distribution with various values of Frank-Kamenetskii parameter λ.

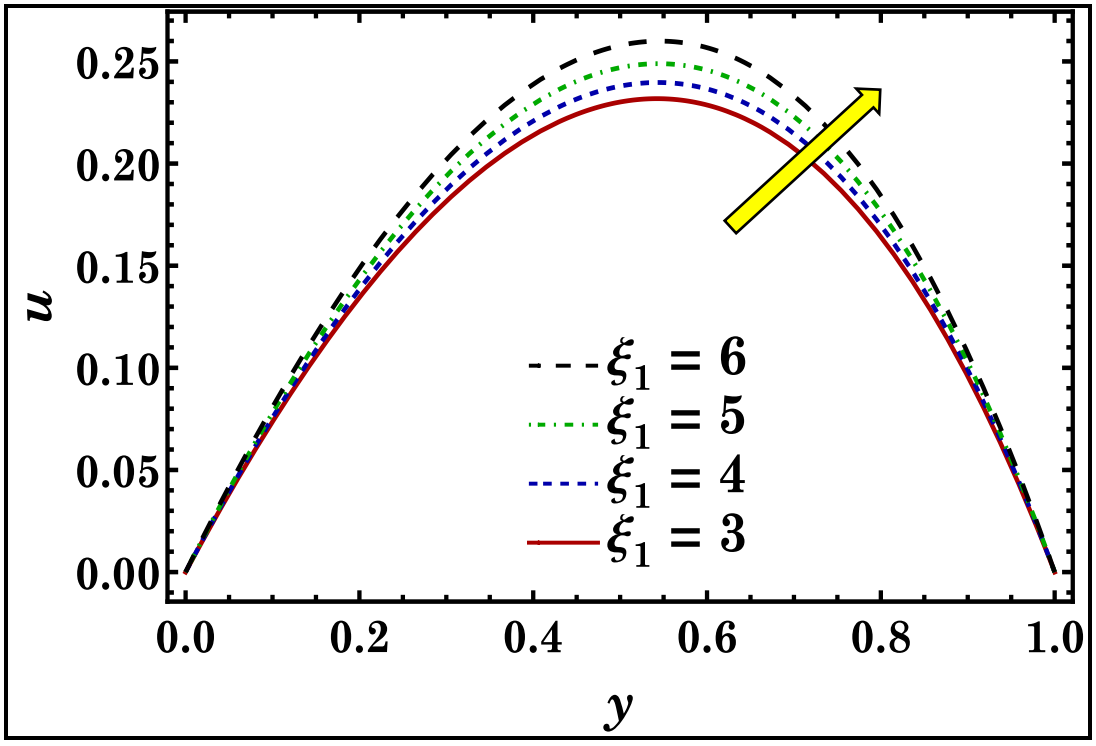

Figure 11: Velocity distribution with influence of Brinkman number ξ_1.

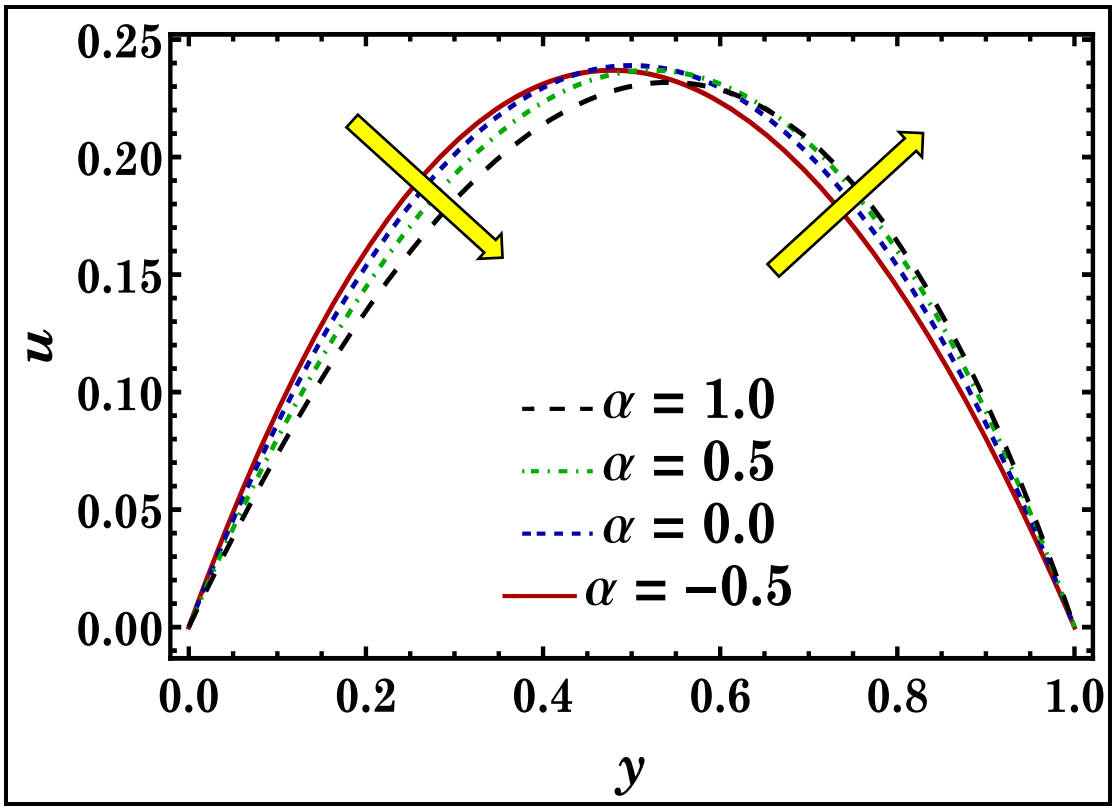

Figure 12: Velocity distribution with suction/injection parameter α.

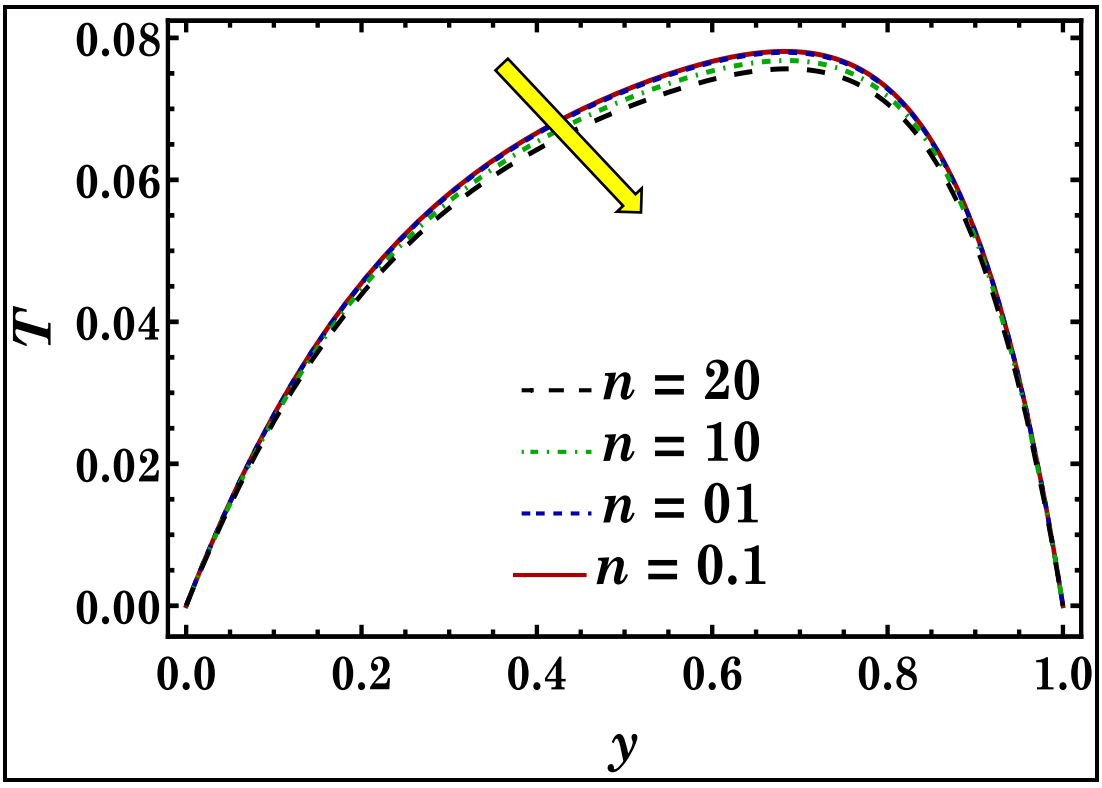

Figure 13: Temperature distribution with Carreau rheological power-law index n.

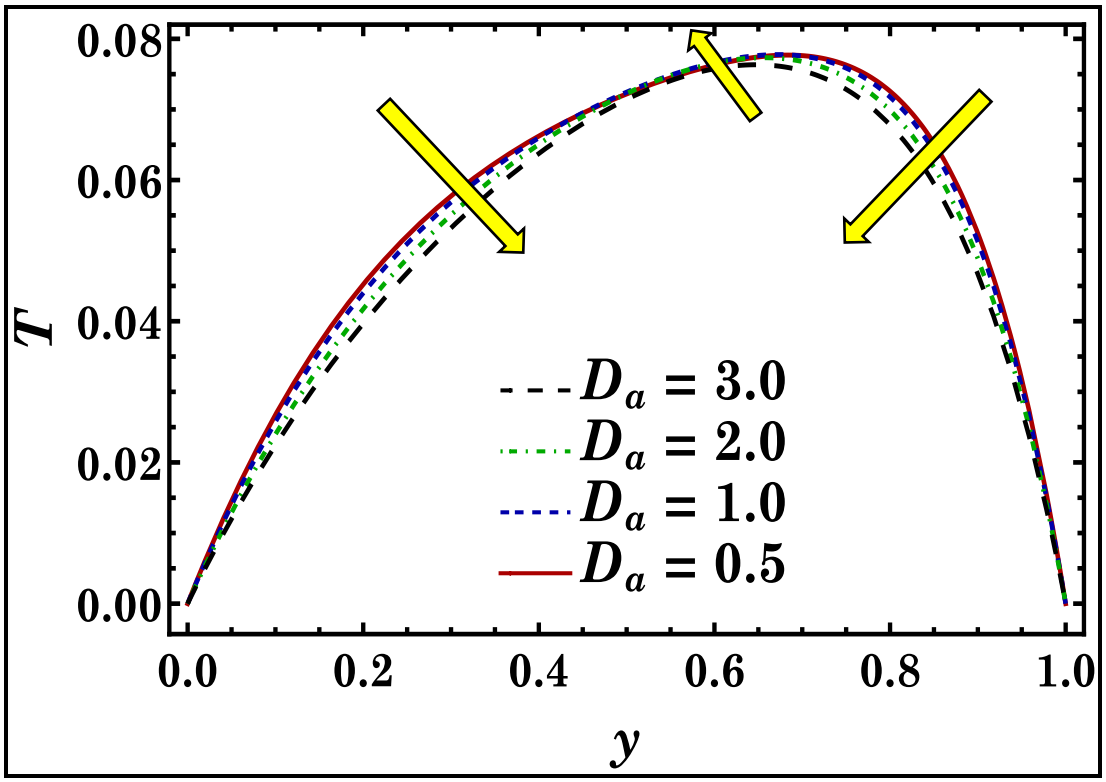

Figure 14: Temperature distribution with Darcy number D_a.

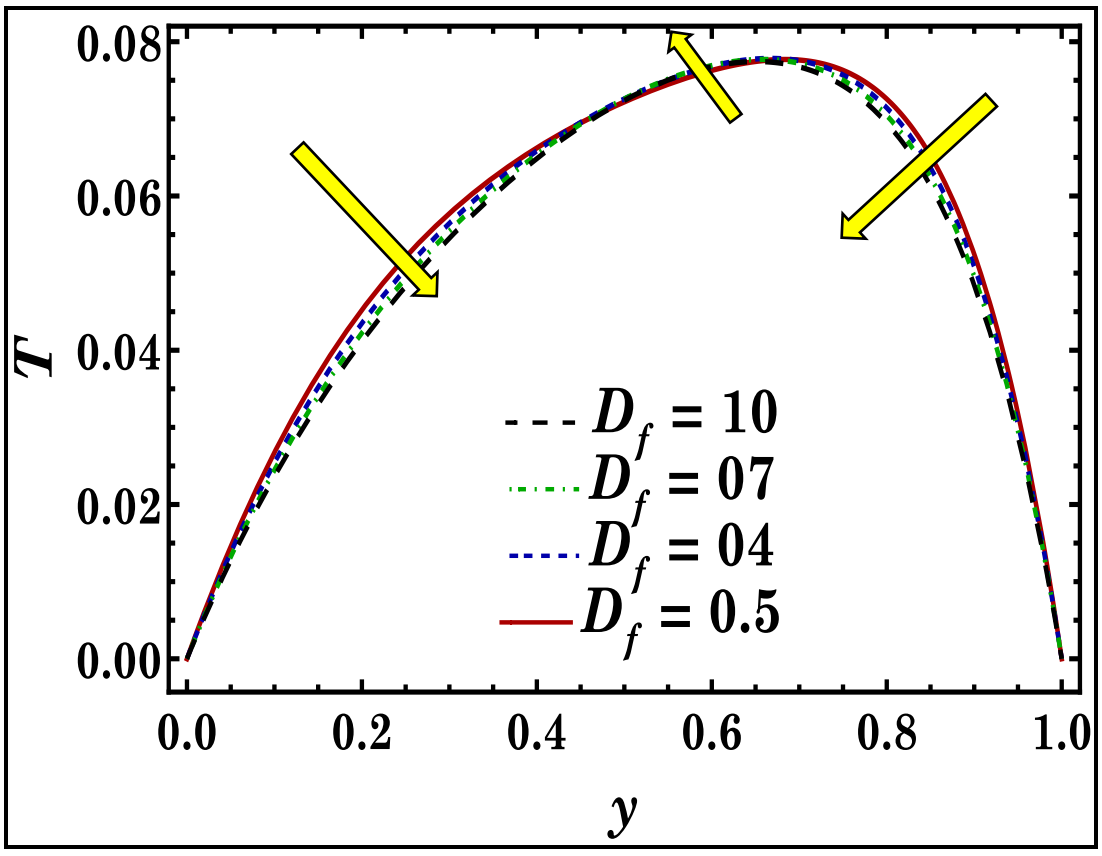

Figure 15: Temperature distribution with Forchheimer number D_f.

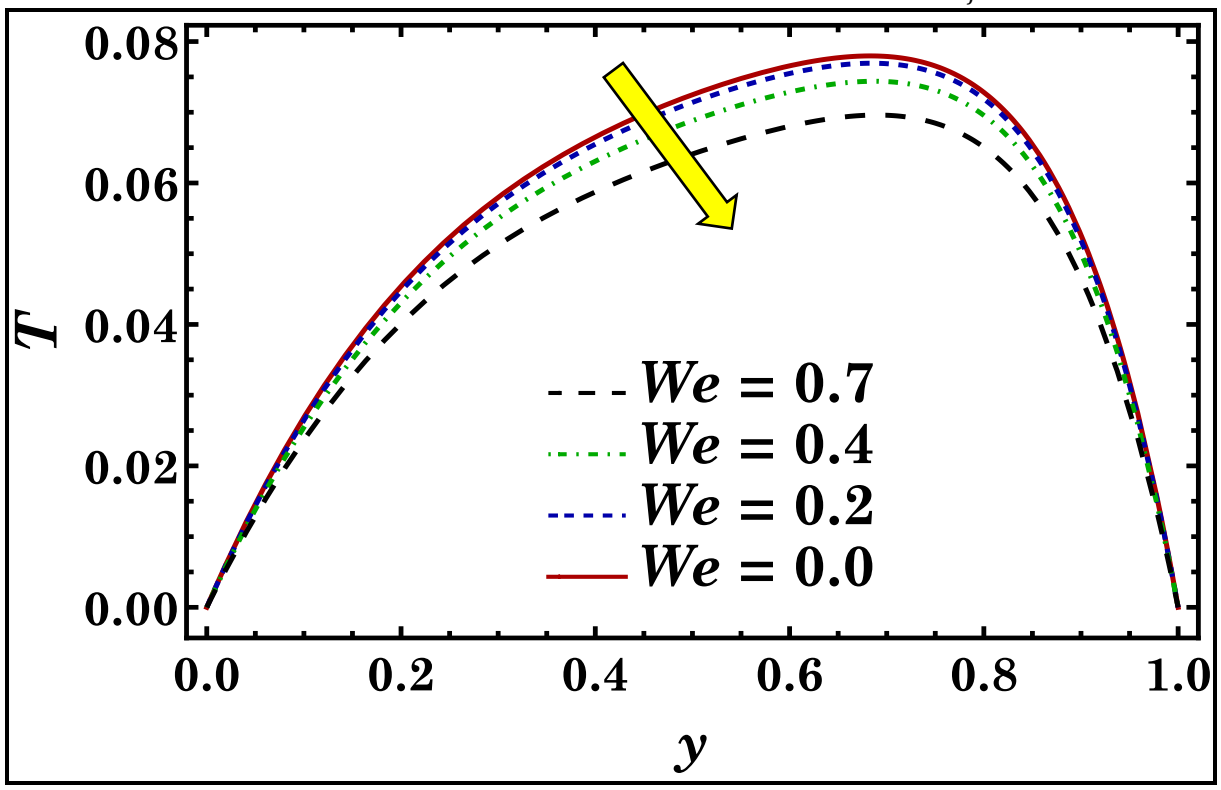

Figure 16: Temperature distribution with Weissenberg number We.

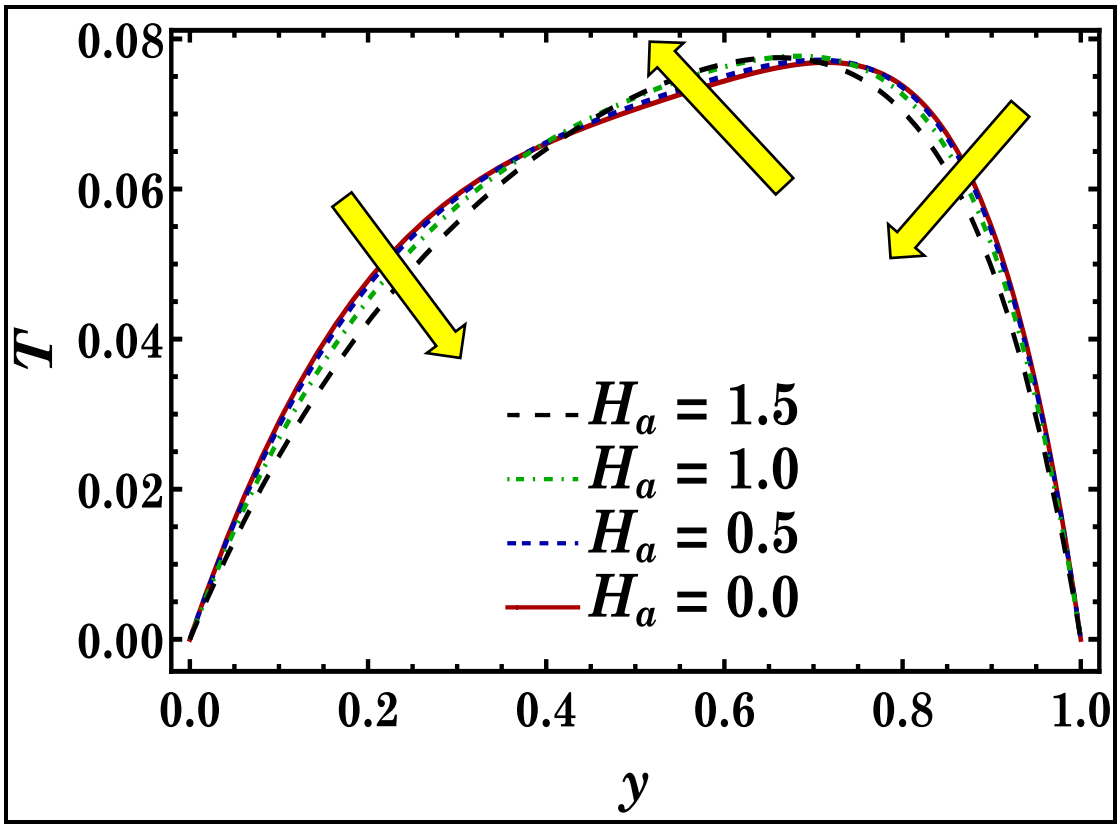

Figure 17: Temperature distribution with Hartmann number H_a.

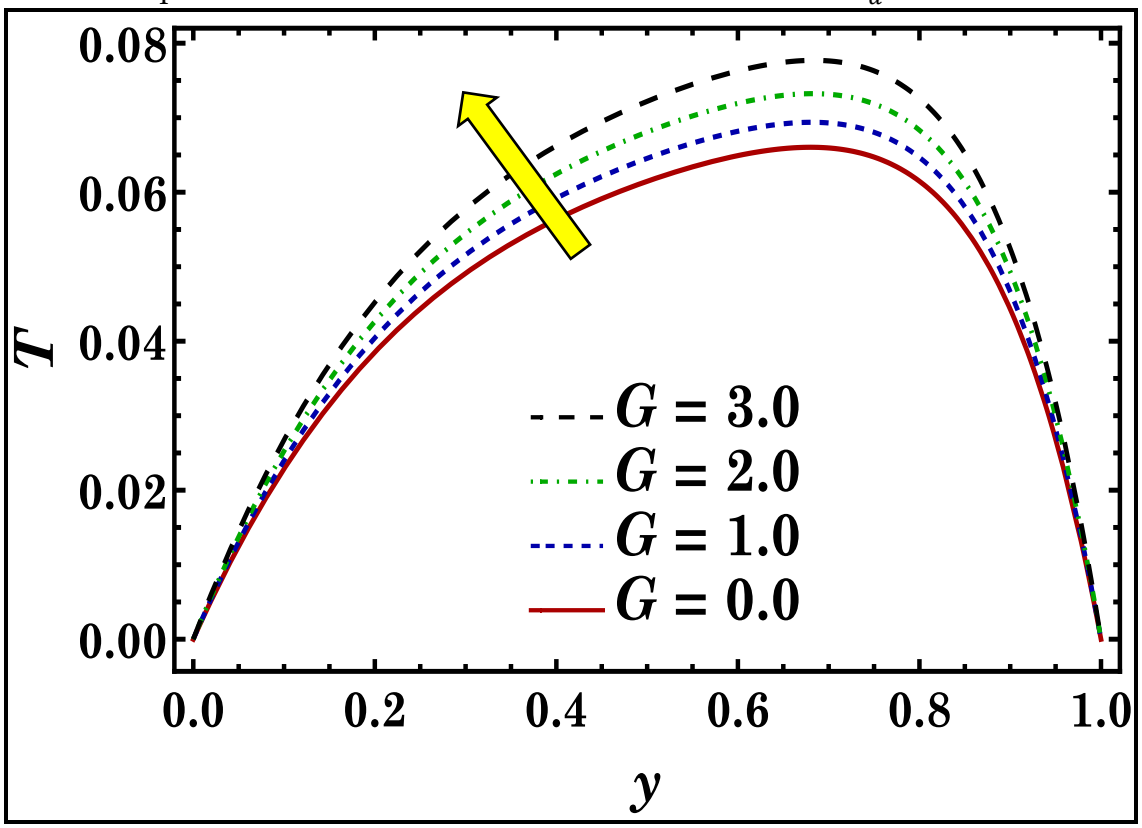

Figure 18: Temperature distribution with Grashof number G.

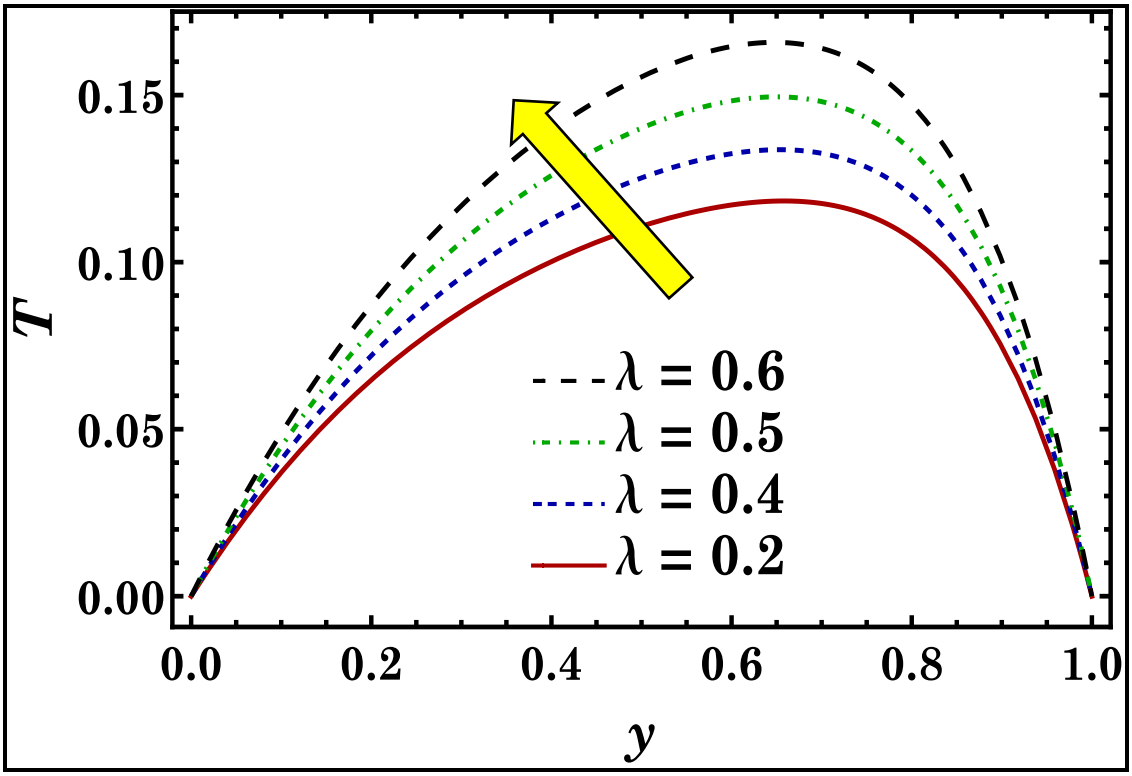

Figure19: Temperature distribution with Frank-Kamenetskii parameter λ.

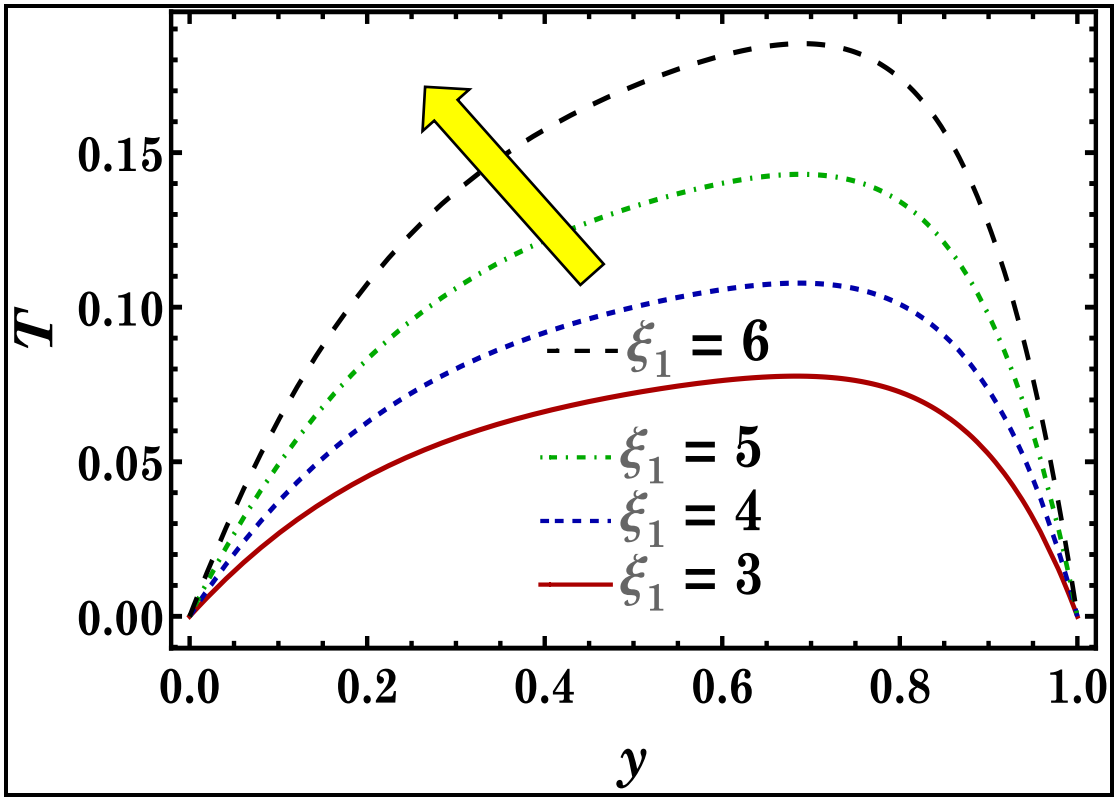

Figure 20: Temperature distribution with Brinkman number ξ_1.

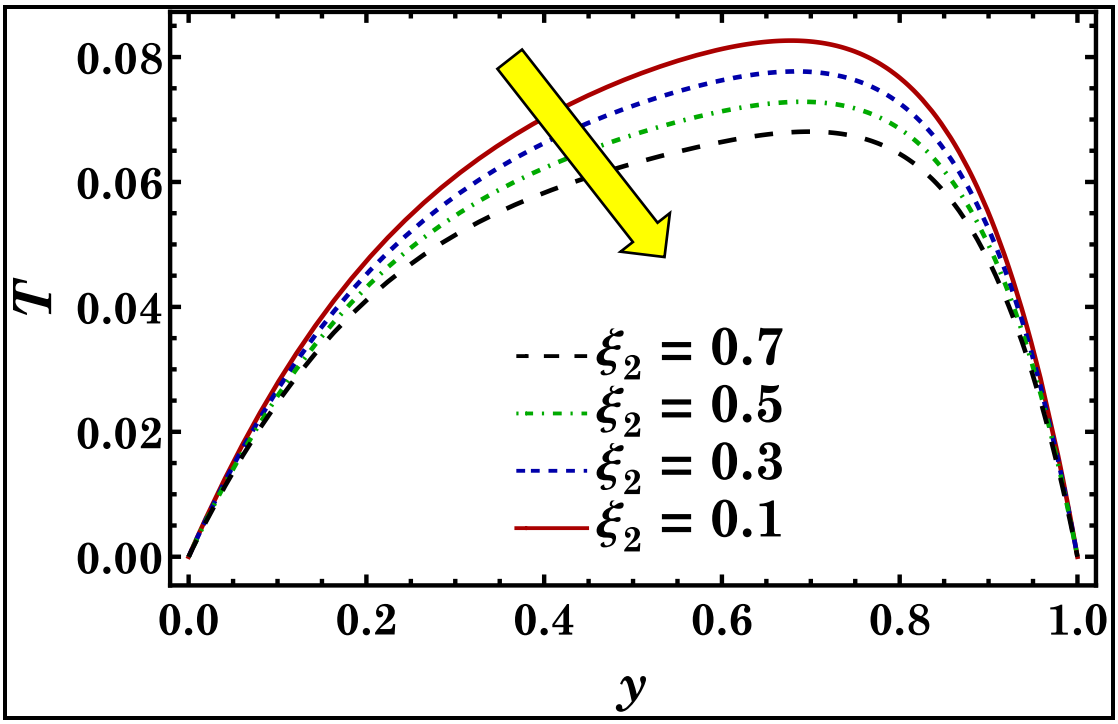

Figure 21: Temperature distribution with heat generation parameter ξ_2.

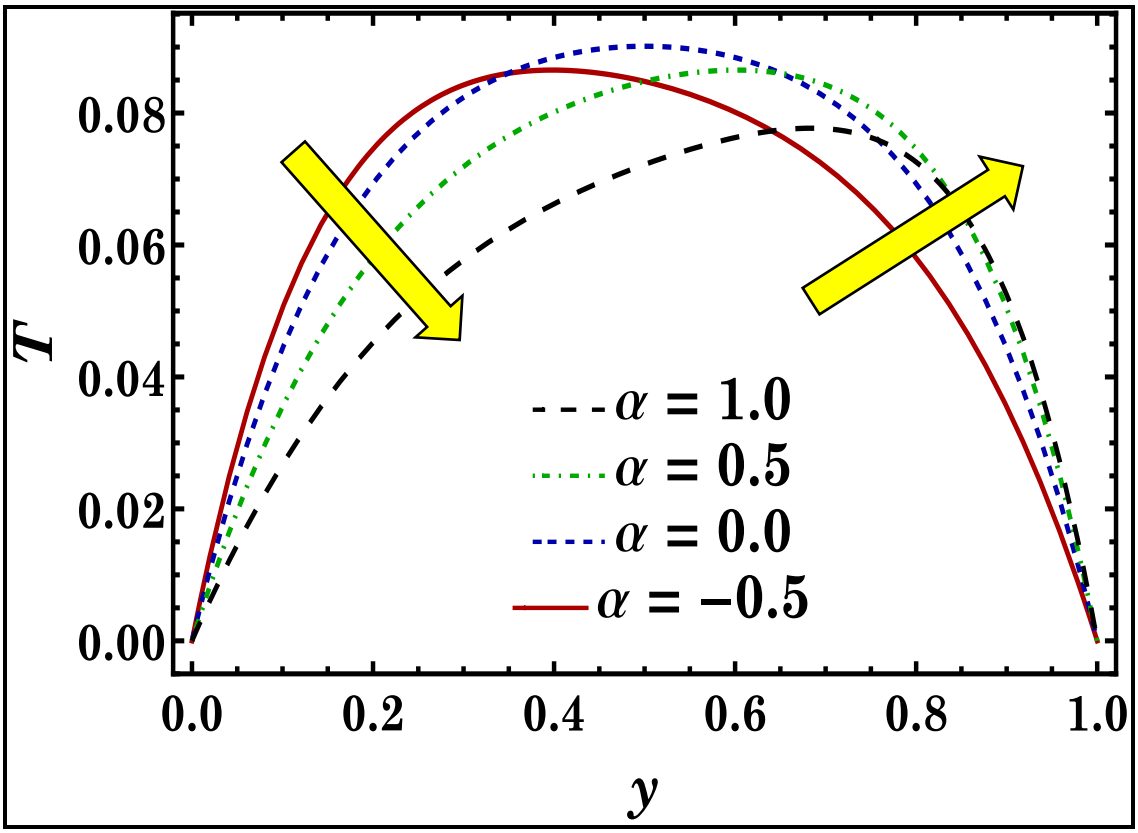

Figure 22: Unveiling temperature variations by exploring the effect of suction/injection α.

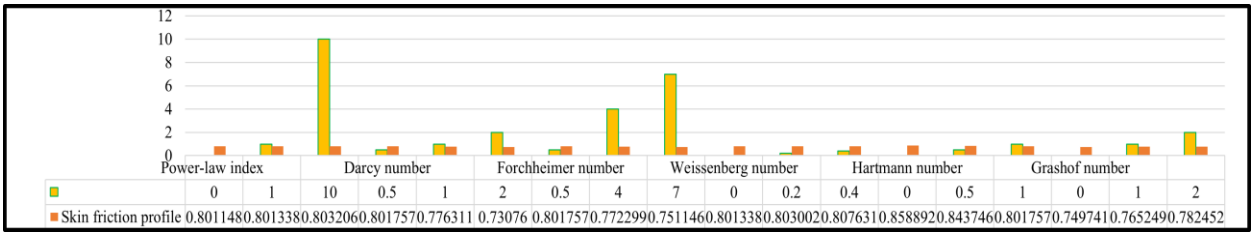

Figure 23: Skin friction profile for different values of Carreau rheological power law index n, Darcy number D_a, Forchheimer number D_f, Weissenberg number We, Hartmann number H_a and Grashof number G.

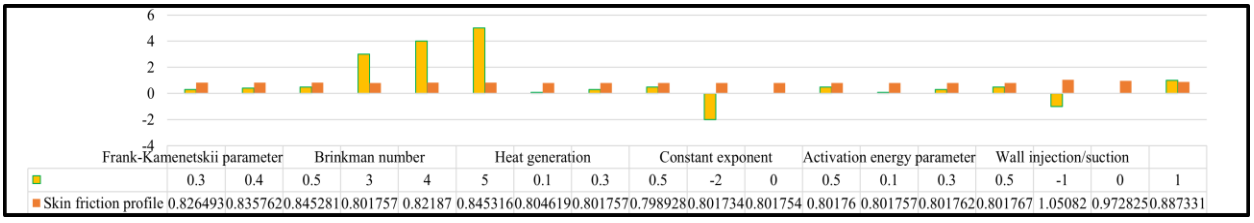

Figure 24: Skin friction profile for different values of Frank-Kamenetskii parameter λ, Brinkman number ξ_1, heat generation ξ_2, exponent m, activation energy parameter β_r and wall injection/suction α.

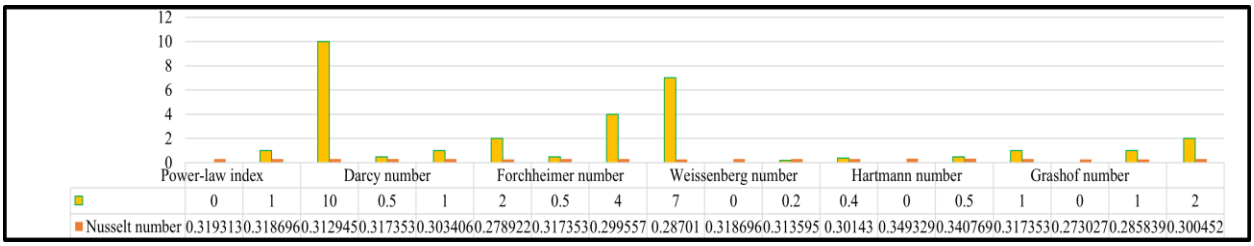

Figure 25: Nusselt number profile for for different values of rheological power-law index n, Darcy number D_a, Forchheimer number D_f, Weissenberg number We, Hartmann number H_a and Grashof number G.

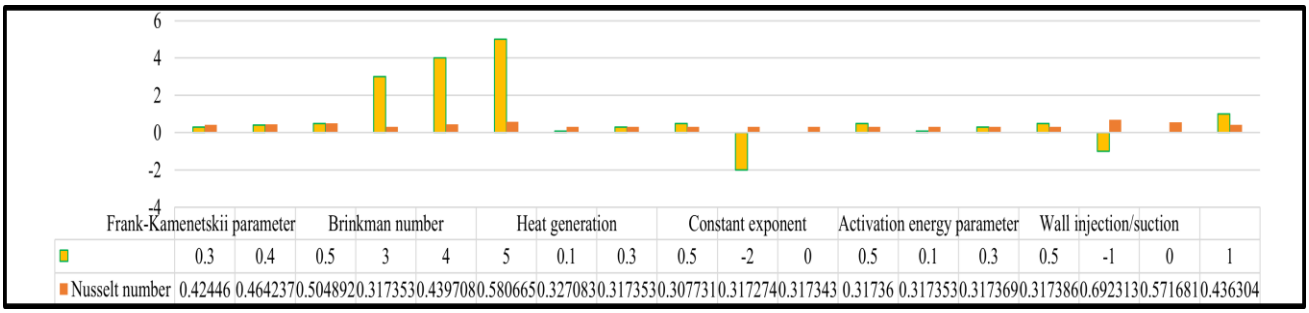

Figure 26: Nusselt number profile for for different values of Frank-Kamenetskii parameter λ, Brinkman number ξ_1, heat generation ξ_2, exponent m, activation energy parameter β_r and wall injection/suction α.

4.1 Velocity profiles

Variations of velocity profile are depicted for different values of rheological power law index n, Darcy number D_a, Forchheimer number D_f, Weissenberg number We, Hartmann number H_a, Grashof number G, Frank-Kamenetskii parameter λ, Brinkman number ξ_1 and suction/injection parameter α in **Figures 4-12**.

It is evident from **Figure 4** that by increasing the power-law index, the velocity profile decreases. The velocity distribution is plotted for three different behaviors: *shear-thinning* $0 < n < 1$, *Newtonian* $n = 1$, *and shear-thickening* $n > 1$. For n *<1*, pseudoplasticity is present indicating that viscous shear resistance in the fluid is diminished. This manifests in axial flow acceleration in the duct. This trend concurs with the findings of Yoon *et al.* [**67**] on gel shear-thinning gel propellants. A noticeable asymmetry is observed in the inverted parabolic profiles with skweness towards the upper duct wall ($y = 1$) i.e. the peak veocity arises some distance into the upper half space rather than along te centre line. This is attributable to the presence of wall

suction at the duct which displaces the peak from the centreline. As n is increased the pseudoplasticity of the fluid is increased and viscosity is curtailed. Clearly strong dilatancy (n > 1), produces the reverse effect i.e. induces deceleration, and this is amplified in the core zone across the channel cross-section. Clearly momentum distributon in the duct is markedly influenced by the rheological nature of the gel. Designers can therefore manipulate the duct gel fluid dynamics and therefore the propulsion effeciency by modifying the characteristics of the gel via shear thinning/thickening. **Fig. 4** also shows the comparison of the NDSOLVE solution with the ADSIM solution for the case n = 0.1. Very close correlation is observed further confirming the accuracy of both approaches. Newtonian gels (n = 1) clearly achieve intermediate velocity in between the pseudoplastic (n = 0.1) and dilatant cases (n =10). As noted in Padwal *et al.* [**24**] and Rahimi *et al.* [**27**], the classical Newtonian model however is inadequate for correctly representing the actual rheology of gel propellant lqiuids. This is confirmed in our results which indicate that Newtonian liquids either over-predict flow acceleration relative to dilatant liquids (n > 1) or under-predict velocityy magnitudes relative to pseudoplastic liquids (n < 1). Despite the strong flow deceleration induced there is never any backflow i.e. flow reveral never arises anywhere in the duct.

Figure 5 visualizes the evolution in velocity across the duct cross-section with Darcy number.The permeability effect is simulated via the Darcy number. In the present model a modified formulation has been deployed in which porous media effects are simulated in both the momentum (14) and heat eqns. (15) following Al Hadrahmi *et al.* [**75**].This invokes Darcian contributions not only in the momentum eqn. (14) but also in the energy eqn. (15). These terms are respectively, $-\left[1+\left(We\frac{du}{dy}\right)^2\right]^{\frac{n-1}{2}} D_a u$ i.e. the modified linear term in the former (14) and an additional *quadratic* term, $+\left[1+\left(We\frac{du}{dy}\right)^2\right]^{\frac{n-1}{2}} \xi_1 D_a u^2$ in the latter (15). The classical model is captured only in the momentum field whereas a new contribution is observed on the temperature field (discussed later). $D_a = \frac{h^2}{k}$ is actually an inverse Darcy number since it is inversely

proportional to the medium permeability. As *Da* is increased, medium permeability is reduced and the Darcian drag force in the momentum eqn. (14) will be diminished. This manifests in a supression (damping) in axial velocity in the duct. Again the profiles are skewed (at all Darcy numbers) towards the upper duct. Maximum flow velocity is computed off-centre. A modification in porous medium permeability therefore clearly achieves a significant alteration in the flow distribution in the duct, encouraging the use of porous materials in for example in liquid rocket fuel gel injector applications [**34, 36**]. The duct flow velocity is damped strongly with lower permeabilities since greater concentration of solid fibers are present for this scenario. This ramps up the impedance to the percolating electromagnetic Carreau fluid inhibiting momentum development and achieving excellent flow control. Again negative velocity is never observed anywhere in the duct i.e. flow reversal is never present.

Figure 6 displays the influence of Forchheimer (inertial porous drag) number on the evolution in velocity across the duct cross-section ($0 \leq y \leq 1$). This parameter, $D_f = \frac{c_f v_0 h^2}{\nu\sqrt{k}}$, features not only in the momentum eqn. (14) (as in conventional Darcy-Forchheimer-Brinkman models) via the classical quadratic term, $-D_f u^2$, but also in the heat eqn. (15), in the cubic term, $+\xi_1 D_f u^3$. With increment in D_f there is a substantial corresponding elevation in Forchheimer impedance which leads to a decrement in axial velocity. When $D_f \to 0$, Forchheimer effects are negated and the Darcy model is retrieved. There are however 4 confirmed regimes in porous medium hydrodynamics. These have been elaborated in detail by for example, Scheidegger [**38**]. The initial regime when inertial forces are totally dominated by viscous forces and the local geometry of the porous medium dictates the velocity behaviour is known as the creeping or Darcy regime. The accepted limit for this regime is pore Reynolds numbers of *up to unity*. When unity value of pore Reynolds number is achieved, the flow is characterized by the emergence of boundary layers in the vicinity of the solid boundaries of the pores within the permeable material. As pore Reynolds number grows up to around 10, with greater momentum development, these boundary layers

also grow and an inertial core to the flow develops. This is usually defined as the *inertial regime*. This results in a departure from the lienar Darcy law to a nonlinear relationship between prssure gradient and flow rate, and is attributable to the Forchheimer drag and steady flow can be maintained upto pore Reynolds numbers of around 150. At this stage a third regime emerges which is sustained upto pore Reynolds number of 300 and may be termed the *unsteady laminar nonlinear regime* characterized by periodic behaviour of the wake zones of the pores and the shedding of vortex structures from around pore Reynolds numbers of 250 up to 300. A fourth and final regime is present for pore Reynolds number exceeding 300 which features increasingly time-dependent chaotic effects and the emergence of turbulent behaviour. As Forchheimer number is enhanced, the peak velocty is displaced progressively closer to the right duct wall ($y = 1$). Backflow does not feature in the duct however even at very high Forchheimer numbers.

Figure 7 depicts the distribution in axial velocity in the duct with modification in Weissenberg number. The Weissenberg number $We = \frac{\Gamma v_0}{\underline{h}}$ and is required to simulate the nonlinear relation between shear stress and strain rate in the non-Newtonian propellant. The electromagnetic gel may be characterized by the ratio of elastic forces to viscous forces. Furthermore, it denotes the proportion between the relaxation time of the fluid and a certain time. When the *Weissenberg* number is very high, the fluid relaxation period will considerably surpass the time scale of the flow, resulting in the predominance of elastic stresses. The occurrence of reverse behavior is seen when the time scale of the flow surpasses the relaxation period, leading to a dominance of viscous effects and a decrease in elastic effects. As a result of reducing the *We*, the fluid experiences less tensile stress impedance, leading to an observed acceleration in axial flow. Specifically, a lower *We* value corresponds to a higher estimated axial velocity. *Weissenberg* arises in multiple terms in the dimensionless momentum eqn. (14), $+\left[1+\left(We\frac{du}{dy}\right)^2\right]^{\frac{n-1}{2}}\frac{d^2u}{dy^2},(n-1)\left(We\frac{du}{dy}\right)^2\left[1+\left(We\frac{du}{dy}\right)^2\right]^{\frac{n-3}{2}}\frac{d^2u}{dy^2},-\left[1+\left(We\frac{du}{dy}\right)^2\right]^{\frac{n-1}{2}}D_a u$. It exerts a profound influence on the shear stress-strain

characteristics of the fluid. When $We \to 0$, the classical Newtonian case is retrieved, and elastic effects are eliminated in the regime. As in other plots, distributions are skewed towards the duct wall at $y = 1$ and no instability is observed in profiles even at high *We*. Although power-law rheological effects have been examined in rocket gel propellants by several authors [**23-28**], they have not explicitly addressed Weissenberg number. Although our simulations are of course limited to laminar flow, nevertheless they provide at least some foundation for future extension to turbulent cases, which are being presently explored with ANSYS FLUENT software and other codes.

Figure 8 illustrates the impact of Hartmann (magnetic) parameter on axial velocity profiles. This parameter is defined as $H_a^2 = \frac{\sigma \underline{h}^2 B_0^2}{\mu}$ and arises in the single linear Lorentz drag term, $-H_a^2 u$ in eqn. (14). When $M = 0$ magnetic field effects vanish, and the gel becomes electrically non-conducting. This produces the maximum flow acceleration in the duct since magnetic drag is not present. As *M* increases there is a strong damping effect on the velocity field. Peak velocity migrates gradually closer to the right duct wall (y =1) with increment in magnetic field intensity (higher Hartmann number). For $M = 1$ the Lorentzian and viscous forces are exactly balanced in the duct (Hartmann number expresses the ratio of these forces). Asymmetry of the velocity distributions is again present at all *M* values. Even with strong magnetic field present (Ha = 1.5), however, flow reversal is not induced in the duct.

Figure 9 depicts the impact of thermal Grashof number, *G*, on velocity profiles. This is another critical parameter influencing the flow characteristics in the duct. $G = \frac{g\beta \underline{h}^2 T_c \beta_r}{\nu v_0}$ and expresses the relative contribution of thermal buoyancy force to viscous hydrodynamic force in the regime. When $G = 0$ natural convection effects are negated and forced convection is present. The thermal buoyancy force, $+G\theta$, therefore vanishes in eqn. (14) and momentum diffusion is no longer affected by the temperature field. This leads to a significant deceleration in the duct flow, across the entire cross-section ($0 \leq y \leq 1$)). As *G* is increased, significant momentum is imparted to the vertical duct flow via natural convection currents which produces strong axial

flow acceleration. Peak velocity is therefore associated with maximum value of G (= 3.0). There is no oscillatory nature to the flow, steady responses are sustained at any value of G across the duct. This is not to say that topologies will not be affected at much higher G values (>100). However in the present study we have confined attention to relatively weak thermal buoyancy effects.

Figure 10 depicts the response in axial duct velocity to variation in the Frank-Kamenetskii parameter. In the present regime, density differences within the electromagnetic gel fluid mobilize natural convection which is produced by the release of heat of an exothermic reaction and this in turn affects the rate of the reaction. This complex interaction between convection and reaction can lead to instabilities observed in reacting duct flows. The Frank-Kamenetskii parameter $\lambda = \frac{\mathcal{Q}\mathcal{S}\mathcal{A}\overline{E}\underline{h}^2\overline{K}^n\underline{T_c}^n\exp\left(-\frac{1}{\beta_r}\right)}{\nu^n\mathcal{L}^n\underline{T_c}^2\overline{R}\kappa}$ *is an exponential parameter* and does not feature explicitly in the momentum eqn. (14). However it appears in the energy eqn. (15) in the term, $+\lambda(1+\beta_r\theta)^m\exp\left(\frac{\theta}{1+\beta_r\theta}\right)$. Via the thermal buoyancy coupling term, $+G\theta$, in eqn. (14), therefore the exothermic reaction exerts an indirect influence on the velocity field. This assists momentum development and generates a marked flow acceleration in the duct. Maximum flow velocity therefore corresponds to largest value of Frank-Kamenetskii parameter since the stronger the exothermic reaction, the more intensified the flow field. This confirms the benefits of using energetic materials with reactive properties in gel propellant design [**34**].

Figure 11 visualizes the evolution in velocity across the duct span with different values of Brinkman number, ξ_1. It features in a number of linear and nonlinear terms in the energy eqn. (15), $+\xi_1\left[1+\left(We\frac{du}{dy}\right)^2\right]^{\frac{n-1}{2}}\left(\frac{du}{dy}\right)^2, +\xi_1 H_a^2u^2, +\left[1+\left(We\frac{du}{dy}\right)^2\right]^{\frac{n-1}{2}}\xi_1 D_a u^2, +\xi_1 D_f u^3$. The first of these terms, $+\xi_1\left[1+\left(We\frac{du}{dy}\right)^2\right]^{\frac{n-1}{2}}\left(\frac{du}{dy}\right)^2$ corresponds to viscous heating. The second term is associated with magnetic Ohmic (Joule) dissipation, $+\xi_1 H_a^2u^2$. The third term, $+\left[1+\left(We\frac{du}{dy}\right)^2\right]^{\frac{n-1}{2}}\xi_1 D_a u^2$ is connected to

Darcy dissipation effects in the porous medium. The final term, $+\xi_1 D_f u^3$ relates to Forchheimer non-linear dissipation effects. [It is very important to note that the magnetic Joule dissipation relates to ξ_1 (Brinkman number) whereas the electrical Joule dissipation, relates to the parameter, $\xi_3 = \frac{\sigma E^2 \underline{h}^2}{\underline{T_c} \kappa \beta_r}$ (described later in the discussion on temperature profiles)]. All these four terms will contribute to a modification in velocity field also due to the very strong coupling via the free convection thermal buoyancy term, $+G\theta$, in eqn. (14). $\xi_1 = \frac{\mu v_0^2}{\kappa \underline{T_c} \beta_r}$ and embodies the relative contribution of viscous effects to heat conduction effects in the duct. It can also be considered as representing the ratio between heat generated via viscous dissipation and heat conveyed through molecular conduction. Larger Brinkman number indicates that thermal conduction is slower due to viscous heating and temperatures are higher. Smaller Brinkman number implies faster thermal conduction and lower temperatures. A significant elevation in velocity corresponds to an increase in Brinkman number. Even though the conventional interpretation is that kinetic energy is destroyed with strong viscous heating, the other contributions from Joule heating and Darcy and Forchheimer effects in fact dominate and this results in a net flow acceleration. The behaviour of the gel propellant in the presence of electromagnetic fields and porous media is therefore very different to characteristics computed in classical thermal convection of purely viscous fluids. Velocity is minimized in the duct with minimal Brinkman number (ξ_1=3) and vice versa for maximum Brinkman number (ξ_1=6). Peak velocity migrates towards the right duct (y =1) with increment in Brinkman number. Clearly the contribution of dissipation effects is significant. Exclusion of these effects in the mathematical model leads to a substantial under-prediction in axial velocity and of course incorrect estimates in temperature magnitudes (discussed later). Propulsion designers therefore are recommended to include viscous heating effects in achieving more robust estimates of flow and thermal characteristics in duct systems.

Figure 12 plots the distribution in axial velocity in the duct (channel) for the ifnleucne of wall transpiration i.e. suction or injection (α). $\alpha < 0$ correponds to suction

and $\alpha < 0$ is associated with wall injection (blowing). Unlike the other velocity distributions, a dual influence is computed in the two half spaces of the duct. In the left hapf space approximately, axial velocity is maximized with suction at that wall whereas strong flow deceleration is induced with injection. A cross-over effect is however computed in the early zone of the rigth half space (around y ~0.6) in which suction decelerates the flow whereas injection accentuates it. The transpiration effect is not modelled via the duct wall boundary conditions, and is instead simulated via the modified velocity gradient term in the momentum eqn. (14), viz, $\alpha\frac{du}{dy}$ and the modified temperature gradient term in the heat eqn. (15), viz, $\alpha\mathrm{Pr}\frac{dT}{dy}$. This creates strong asymmetry in the flow field. Effectively different flow characteristics can be generated in the electromagnetic gel duct regime via manipulating these terms. Physically suction will corespond to a stronger adherence of the duct wall boundary layer to the wall due to the systematic removal of fluid via pores, whereas injection will introduce supplementary fluid into the duct. These techniques are also of great use in manipulating heat transfer rates and achiving cooling at the duct walls, as will be described shortly. The injection effect is markedly stronger in the left half space than the right half space even with the same values of positive α.

4.2Temperature distributions

Temperature profiles computed with the Mathematica NDSOLVE routine are visualized in **Figs. 13- 22**. The influence of rheological power-law index n, inverse Darcy number D_a, Forchheimer number D_f, Weissenberg number We, Hartmann number H_a, Grashof number G, Frank-Kamenetskii parameter λ, Brinkman number ξ_1, suction/injection parameter α and heat generation parameter ξ_2 are examined.

Figure 13 demonstrates that when the Carreau power-law index (n) is elevated, the ttemperature magnitudes are consistently reduced, primarily in the core region of the duct. Although the parameter, n, is a hydrodynamic parameter, it features, as noted earlier also in the temperature eqn. (15), in the terms, $+\xi_1\left[1+\right.$

$\left(We\frac{du}{dy}\right)^2\Big]^{\frac{n-1}{2}}\left(\frac{du}{dy}\right)^2$, $+\left[1+\left(We\frac{du}{dy}\right)^2\right]^{\frac{n-1}{2}}\xi_1 D_a u^2$. *It therefore exerts a direct effect on temperature field by virtue of the Carreau non-Newtonian formulation and modified porous media model utilized here.* In many other studies this effect has been ignored and confined only to the momentum eqn. (14), see for example Yoon *et al.* [**67**]. Similar to the velocity response, an increment in power-law index suppresses temperatures. Shear-thinning fluids (n = 0.1 i.e weakly pseudoplastic) attain the maximum temperature across the duct cross-section. Strongly dilatant liquids produce a cooling effect and the lowest temperatures. Newtonian liquids are associated with slightly lower temperatures than the pseudoplastic case, but significantly greater temperatures than the dilatant case, in particular in the core region of the duct. Thermal characteristics of the propellant are therefore non-trivially influenced by the rheology, an observation which has also been made by Arnold *et al.* [**25**] who consider JP-8 and RP-1 fuels and utilized a Herschel-Bulkley model. However they neglected viscoelastic charecteristics, specifically Weissenberg number effects which have been considered for the first time in the present study.

Figure 14 visualizes the influence of inverse Darcy number on temperature evolution in the duct. The response is varied across the channel cross-section. In the left half-space and right half space, increment in D_a strongly suppresses temperatures; however in a small section of the core zone it has the opposite effect, although much weaker. As elaborated earlier, with the modified non-Darcy model formulation, a supplementary terms appears in the energy eqn. (15), viz, $+\left[1+\left(We\frac{du}{dy}\right)^2\right]^{\frac{n-1}{2}}\xi_1 D_a u^2$ which is quadratic in velocity. Since an inverse Darcy number is used which is larger for smaller permeability and smaller for larger permeability of the porous medium, the implication is that larger D_a values will produce a reduced concentration of solid fibers in the porous medium. This will deplete thermal conduction and reduce temperatures i.e. colling will be induced. Minimal temperatures will therefore be produced in the duct for highest inverse Darcy number and vice versa. To maximize temperatures in the duct, more densely packed porous media are required which

correspond to higher inverse Darcy numbers (lower permeability). In the core zone, a slight anomoly arises where there is a brief elevation in temperature with lower inverse Darcy number. However the dominant effect across the duct is sustained very quickly afterwards in the right half space. Strong skewness in the temperature profiles towards the right duct ($y = 1$) is apparent, which again is due to the presence of suction/injection ($\alpha \neq 0$). Th eprimary influence of inverse Darcy number is on the momentum characteristics and indirectly via the coupling term, this is exerted on the temperature field. Jeigarnik *et al.* [**35**] have also noted this characteristic in their study of porous media deployment in rocket duct propulsion systems.

Figure 15, visualizes the evolution in temperature across the duct span with Forchheimer number. Agan there is a general decay in temperatures with increment in Forchheimer number, D_f. The minimum temperature is computed with maximum D_f of 10 and the maximum temperature correspond to the weak inertial drag case ($D_f = 0.5$). Profiles are warped towards the right duct wall ($y = 1$) at all D_f values. A weak increase in temperature with larger D_f is computed near the centre-line. While not present in traditional Darcy-Brinkman-Forchheimer drag force models, the impact of D_f in the present model is simulated directly in the energy eqn. (15), via the cubic velocity term, $+\xi_1 D_f u^3$. A small change therefore in velocity will be amplified cubically to influence the temperature distribution. There is also a significant interplay between velocity and thermal fields due to the presence of viscous and Joule dissipation. This also contributes increasingly to the net impact of Forchheimer drag especially at higher velocities in the duct.

Figure 16 depicts the influence of the gel viscoelastic parameter, Weissenberg number (We) on temperature distributions. Unlike the response to inverse Darcy number, Forchheimer number or rheological power-law index, there is a consistent decrease across the enture duct with increasing Weissenberg number. The Newtonian case ($We = 0$) achieves the greatest temperatures. Stronger elastic forces in the regime therefore contribute to a significant cooling effect which is beneficial for thermal management in rocket duct applications. Weakly elastic or vanishing elastic effects lead to higher temperatures. Galecki [**26**] has noted that the viscoelastic

nature of rocket gels can be manipulated by doping with specific metallic particles. These simultaneously contribute to thermal ignition but do not interfere with the gel rheology or induce clogging and agglomeration effects. Arnold *et al.* [**25**] have also recommended a combined design using the smallest possible storage volume via metallic particles (oxidizers) in combination with energetic gels produces the best propulsion performance. They have highlighted the benefits of silica as the gelling agent which is also tactically useful for adjusting viscosity of the gel propellant and can be exploited to control the heat of vapirozation during ignition.

Figure 17 illustrates the impact of Hartmann (magnetic) number, Ha, on temperature plots. In the left and right half space extremities, surrounding the core zone, temperature is strongly reduced with an increment in magnetic field instensity. However a distinct zone does arise in the core region of the duct where the classical response in temperature is captured i.e. a strong enhancement. In this central zone the non-conducting case (Ha =0) produces the minimal temperatures whereas the high magnetic field case generates peak temperatures, which are in fact the highest computed ay any location across the duct span. The principal contributing factor to this temperature elevation in the core zone is the Ohmic dissipation (Joule heating) effect, simulated via the term, ξ_3 in eqn. (15). However this parameter is not the conventional magnetic field generated dissipation term. It is related to the electrical field, as per the definition, $\xi_3 = \frac{\sigma E^2 \underline{h}^2}{\underline{T_c} \kappa \beta_r}$ in eqn. (16) where E is the electrical field. Supplementary work is performed by the electromagnetic gel in dragging itself against the action of the *electrical field*. This work is dissipated via the *Joule electrical resistance* and this leads to heating in the core of the duct and the boost in temperatures. Since in propulsion applications, the core duct characteristics are critical, the inclusion of Ohmic electrical (Joule) heating is as important as magnetic Joule dissipation, since it more accurately predicts the higher temperatures present which are not represented in mathematical models neglecting either electrical Ohmic dissipation (electrical Joule heating) or magnetic dissipation. An under-prediction in temperatures will lead to a reduction in estmated thermodynamic efficiency of the

duct system and also engineers will not be able to properly assess the design temperatures. With excessive temperatures, chemical corrosion effects can be induced in the duct walls due to recirculating heat from the core, which can manifest in serious downtime, efficency drop and other detrimental effects requiring expensive maintenance. High temperature corrosion effects [**24**] can be more robustly appraised with inclusion of Joule dissipation in predictive models.

Figure 18 reveals the response in temperature profiles with modification in thermal Grashof number. The forced convection case (G = 0) produces the minimal temperatures in the duct since natural convection currents (associated with gel density differences) are eliminated. With increasing Grashof number, thermal buoyancy progressively dominates the viscous resistance forces in the regime. This encourages strong thermal diffusion through the duct as hotter gel fluid rises and the cooler gel fluid descends the duct. This exacerbates free convection currents and boosts the temperatures significantly. The peak temperature is always observed in the right half space and is systematically displaced further towards the right duct wall (y = 1) with greater values of G. Skewness in the temperature distributions is therefore also amplified with greater thermal buoyancy effects. The interaction of thrmal buoyancy with porous media effects is also likely to contribute to the significant modification in temperatures, which concurs with the earlier fndings of Seader *et al.* [**76**] on rocket duct heat transmission.

Figure 19 visualizes the influence of the Frank-Kamenetskii parameter (λ) on thermal profiles across the duct span. Significant elevation in temperatures is computed over a relatively small increment in this parameter ($0.2<\lambda<0.6$). As noted earlier, this parameter embodies the ratio of exothermic activation energy to thermal energy in a reactive system. Heat emerges in a reactive system as a result of intensification in exothermic chemical reaction, which energizes the duct and boosts temperatures. This will in turn influence the so-called real duct thermal efficiency which is dependent on viscous properties of the propellant, as documented by Padwal *et al.* [24]. Furthermore, as the Frank-Kamenetskii parameter in the duct is elevated,

the exothermic term, $+\lambda(1+\beta_r\theta)^m \exp\left(\frac{\theta}{1+\beta_r\theta}\right)$ is amplified. This assists the natural convection and optimizes heat transmission. Strong asymmetry in the temperature profiles is clearly captured in all the plots. The peak temperature in the core region of the duct migrates significantly towards the right duct wall with increment in Frank-Kamenetskii parameter (λ). Clearly highly energetic propellants (larger values of Frank-Kamenetskii parameter, λ) are justified since they achieve the maximum temperatures which are highly desirable for propulsion applications.

Figure 20 displays the impact of the Brinkman number (viscous heating parameter) on temperature evolution in the duct. Brinkman number $\xi_1 = \frac{\mu v_0^2}{\kappa \underline{T}_c \beta_r}$, as explained earlier, is not isolated to a single term in the energy eqn. (15). It features in the modified shear term, $+\xi_1\left[1+\left(We\frac{du}{dy}\right)^2\right]^{\frac{n-1}{2}}\left(\frac{du}{dy}\right)^2$, in the magnetic dissipation term, $+\xi_1 H_a^2 u^2$, in the modified Darcy dissipation term, $+\left[1+\left(We\frac{du}{dy}\right)^2\right]^{\frac{n-1}{2}}\xi_1 D_a u^2$ and fnally in the modified Forchheimer inertial dissipation term, $+\xi_1 D_f u^3$. Brinkman number will therefore substantially interplay with the temperature field and very significantly enhances temperatures across the duct span. Internal friction effects are maximized with larger Brinkman number relative to thermal conduction effects. The scenario of a vanishing Brinkman number, $\xi_1 = 0$, clearly correlates to the lowest temperature and indicates that the absence of viscous heating leads to temperature under-prediction in the bulk fluid in the duct. The inclusion of viscous heating in real duct propulsion flows is therefore very important for designers utsing mathematical models.

Figure 21 illustrates the influence of electromagnetic to thermal conduction ratio parameter, $\xi_2 (= \frac{2\sigma B_0 E v_0 \underline{h}^2}{\underline{T}_c \kappa \beta_r})$. Although only present in a single linear velocity term, $-\xi_2 u$ in eqn. (15), it exerts a marked influence on temperature characteristics. Increment In this parameter clearly depletes the temperature magnitudes across the duct. Maximum temperatures are estimated when this parameter disappears, $\xi_2 \to 0$, and thermal conduction dominates over electrical and magnetic field heating

effects. This parameter fundamentally characterizes the impact of heat production on heat conduction inside a duct, arising from the interplay between transverse magnetic and axial electric fields. In the absence of this parameter, specifically when $\xi_2 = 0$, the influence of heat production on thermal conduction resulting from the combined electromagnetohydrodynamic action becomes negligible, leading to the attainment of maximum temperatures. The suggestion is that the aforementioned parameter has a cooling influence on the system, as its rise leads to a reduction in the alteration of thermal conduction caused by the combined action of electrical and magnetic fields. With amplification in this parameter the skewness in temperature profiles is also considerably amplified towards the right duct wall (y = 1). Evidently the minimal temperatures in the duct are achieved for ξ_2 =0.7 and the peak temperature is computed just off-centre with ξ_2 = 0.1.

Fig. 22 plots the distribution in temperature profile across the duct span with variation in the suction or injection parameter (α). Near the left duct wall temperature is maximized with suction (α = -0.5) whereas near the right duct wall it is maximized with strong injection (α = 1.0). In the core region, absence of either suction or injection (α = 0) produces the highest temperatures. Therefore the manipulating of the heat transfer in the duct is possible with alteration in suction and blowing conditions. Strong cooling is achieved only in the left half space with injection and also in the core duct zone; However cooling is only produced in the right half space with suction.

Figs. 23-26 visuailize as histograms the relative influence of all parameters on skin friction, $S_f = \frac{du}{dy}\left[1 + \left(We\frac{du}{dy}\right)^2\right]^{\frac{n-1}{2}}\Big|_{y=0}$ and Nusselt number, $N_u = \frac{dT}{dy}\Big|_{y=0}$ as extracted from **Tables 1 and 2**, at the left duct wall (y = 0). Inspection of these figures shows that the maximum elevation in skin friction corresponds to highest inverse Darcy number followed by maximum Weissenberg number (**Fig. 23**). The other parameters i.e. Carreau rheological power law index n, Forchheimer number D_f, Hartmann number H_a and Grashof number G have a comparatively much reduced impact on

skin friction at the duct wall. **Fig 24** shows that low values of Brinkman number ξ_1 and high values of electromagnetic to conduction heat generation ratio parameter ξ_2, maximize the skin friction. The remaining parameters viz, Frank-Kamenetskii parameter λ, reaction exponent m, activation energy parameter β_r and wall injection/suction α have a relatively lower influence on skin friction. **Fig. 25** shows that again the maximum enhancment in Nusselt number is computed with high values of the Darcy inverse parameter and large values of the Weissenberg number, with other parameters contributing to a much lesser degree. Finally **Fig. 26** indicates that the maximum elevation in Nusselt number (heat transfer from the bulk fluid to the left duct wall) is induced with high values of electromagnetic/conduction heat generation ξ_2, then Brinkman number ξ_1, followed by Frank-Kamenetskii parameter λ. Maximum negative Nusselt number (heat transfer from the left duct wall to the bulk fluid) accompanies highest value of .reactive exponent m followed by wall injection/suction α. High values of the activation energy parameter β_r produce a relatively weak increase in positive Nusselt number.

5.CONCLUSIONS

To study steady, laminar electromagnetic non-Newtonian gel propellant thermo-fluid transport in a vertical duct containing a homogenous porous medium, a mathematical model has been developed. The model includes the composite multi-physical effects of exothermic reaction, non-Darcy porous media drag forces, suction/injection, magnetic Joule dissipation, electrical Joule heating, viscous heating and thermal buoyancy. The Carreau rheological model has been deployed which features both pseudoplasticity/dislatancy of the gel and viscoelastic effects. A modified Darcy-Brinkman-Forchheimer porous medium drag force model with dissipation terms in the energy balance has been utilized. The Frank-Kamenetskii thermal explosion exothermic chemical kinetic model has been implemented for energetic gel propellants. Isothermal duct wall conditions are used. Static uniform axial electrical field and transverse magnetic field is considered. Via scaling transformations, a nonlinear ordinary differential boundary value problem comprising momentum and

energy equations with wall duct boundary conditions is derived. A numerical solution is obtained using the Mathematica-based shooting algorithm (NDSOLVE). Verification with an Adomian decomposition method (ADM) is included demonstrating excellent correlation. Velocity, temperature, duct wall skin friction and Nusselt number are computed for the influence of all key parameters and depicted in graphs and tables. The present simulations have shown that:

(i) An increment in Frank-Kamenetskii parameter strongly elevates bulk gel fluid temperatures and accelerates the duct flow indicating that highly energetic propellants hold promise for rocket propulsion systems.

(ii) Elevation in power-law rheological index and Weissenberg number produces significant damping in the flow and also temperature reduction across the duct, showing that dilatancy and strong elastic force decelerate the gel flow but are advantageous for thermal management in duct propulsion.

(iii) Increasing Darcy number and Forchheimer number suppress temperature magnitudes in proximity to the duct walls but induce a slight heating effect in the core zone. Porous media can therefore be judiviously deployed to manipulate heat transfer characteristics in ducted propulsion.

(iv) A rise in thermal buoyancy parameter i.e. Grashof number accelerate the duct flow and boost temperatures significantly.

(v) Higher magnitudes of magnetic field intensity, as simulated in the Hartmann (magnetic) number suppress temperatures near the duct walls but elevate them in the core region of the duct. Flow deceleration in the core is also computed with higher Hartmann number. Intense magnetic field therefore permits strong flow control but contributes to heating in the duct regime.

(vi) Larger Brinkman number strongly acentuates Nusselt number at the left duct wall.

(vii) Increasing values of electromagnetic to conduction heat generation ratio parameter strongly enhance skin friction at the left duct wall.

(viii) A large elevation enhancment in Nusselt number is computed with high values of the Darcy inverse parameter and large values of the Weissenberg number, with other parameters contributing to a much lesser degree.

(ix) Significant enhancment in Nusselt number (heat transfer from the bulk fluid to the left duct wall) is induced with high values of electromagnetic/conduction heat generation although there is also a strong elevation with increasing Brinkman number and Frank-Kamenetskii parameter (more intense exothermic reaction in the gel propellant).

(x) Maximum negative Nusselt number (heat transfer from the left duct wall to the bulk fluid) accompanies the highest value of .reactive exponent followed by wall injection/suction α.

(xi) High values of the gel activation energy parameter produce a relatively weak increase in positive Nusselt number.

Future work: The present investigation has revealed some intricate hydrodynamic and thermal characteristics associated with electromagnetic rheological gel propellants exploiting exothermic reactions. Attention has however been confined to momentum and Fourier-based conduction heat transfer. Future investigations may address non-Fourier (thermal relaxation) and *mass transfer* (binary species) aspects and explore non-Fickian diffusion involving solute relaxation. Additionally alternative non-Newtonian models may be deployed to represent a wide range of actual gel propellant rheology including finitely extensible nonlinear elastic Peterlin models (FENE-P) [**79**] and Phan-Thein–Tanner (PTT) elastic-viscous models [**80**]. These may also be studied in the context of turbulent duct flows using computational fluid dynamics (CFD) codes with appropriate turbulence closure models e. g. K-epsilon model. It is also noteworthy that the current simulations can also be extended to oscillatory propulsion with full duct rotation [**81**] and hybrid nano-fuels [**82**]. Efforts in these directions are currently underway and will be communicated imminently.

REFERENCES

[1] T. Boddington, C.-G. Feng, P. Gray, "Thermal explosions, criticality and the disappearance of criticality in systems with distributed temperatures. I. Arbitrary Biot number and general reaction-rate laws," *Proc. R. Soc. Lond.*, vol. 390, no. 1799, pp. 247–264, 1983, doi: 10.1098/rspa.1983.0130.

[2] O. D. Makinde and P. Sibanda, "On solution driven flow and heat transfer in a pipe filled with porous media," *Comput. Assist. Mech. Eng. Sci.*, no. Vol. 5, nr 4, pp. 389–398, 1998, Accessed: Sep. 24, 2023. https://www.infona.pl/resource/bwmeta1.element.baztech-article-BPB2-0001-0110

[3] S. K. Som, S. S. Mondal, and S. K. Dash, "Energy and exergy balance in the process of pulverized coal combustion in a tubular combustor," *J. Heat Transfer*, vol. 127, no. 12, pp. 1322–1333, 2005, doi: 10.1115/1.2101860.

[4] H. Ogunseye and S. S. Okoya, "Criticality and thermal explosion in the flow of reactive viscous third grade fluid flow in a cylindrical pipe with surface cooling," *J. Nigerian Math. Soc.*, vol. 36, no. 2, pp. 399–418, 2017, doi: https://jnms.ictp.it/jnms/index.php/jnms/article/view/146

[5] M. Daneshipour and R. Rafee, "Nanofluids as the circuit fluids of the geothermal borehole heat exchangers," *Int. Comm. Heat Mass Transf.*, vol. 81, pp. 34–41, 2017, doi: 10.1016/j.icheatmasstransfer.2016.12.002

[6] D. A. Frank-Kamenetskii, *Diffusion and heat transfer in chemical kinetics*. New York, NY: Kluwer Academic/Plenum, 1995.

[7] N. N. Semenov, The calculation of critical temperatures of thermal explosion. *Z Phys Chem.*, vol. 48, pp. 571, 1928.

[8] C. K. Law and H. K. Law, "Thermal-ignition analysis in boundary-layer flows," *J. Fluid Mech.*, vol. 92, no. 01, p. 97, 1979, doi: 10.1017/s0022112079000537.

[9] S. Li, Q. Yao, and C. K. Law, "Thermal-ignition analysis in wall-bounded boundary-layer flows with an unheated starting length," *Combust. Sci. Technol.*, vol. 190, no. 10, pp. 1722–1737, 2018, doi: 10.1080/00102202.2018.1469131.

[10] O. A. Bég, M.M. Rashidi, M.T. Rastegari, Tasveer A. Bég, S.S. Motsa, Amna Halim, "DTM-padé numerical simulation of electrohydrodynamic ion drag medical pumps with electrical Hartmann and electrical Reynolds number effects," *J. Adv. Biotechnol. Bioeng.*, 2013, doi: 10.12970/2311-1755.2013.01.02.3.

[11] D D. Martínez-Ruiz, J. Urzay, A. L. Sánchez, A. Liñán, and F. A. Williams, "Dynamics of thermal ignition of spray flames in mixing layers," *J. Fluid Mech.*, vol. 734, pp. 387–423, 2013, doi: 10.1017/jfm.2013.500.

[12] O. A. Beg, S. S. Motsa, M. N. Islam, and M. Lockwood, "Pseudo-spectral and variational iteration simulation of exothermically reacting Rivlin-Ericksen viscoelastic flow and heat transfer in a rocket propulsion duct," *Comput. Therm. Sci. Int. J.*, vol. 6, no. 2, pp. 91–102, 2014, doi: 10.1615/computthermalscien.2014010009.

[13] M. S. Hashmi, N. Khan, S. Ullah Khan, and M. M. Rashidi, "A mathematical model for mixed convective flow of chemically reactive Oldroyd-B fluid between isothermal stretching disks," *Results Phys.*, vol. 7, pp. 3016–3023, 2017, doi: 10.1016/j.rinp.2017.08.017.

[14] P. Gordon, "On thermal explosion in porous media," *Nonlinearity*, vol. 23, no. 6, pp. 1433–1447, 2010, doi: 10.1088/0951-7715/23/6/009.

[15] M. M. Rahman, I. Pop, and M. Z. Saghir, "Steady free convection flow within a titled nanofluid saturated porous cavity in the presence of a sloping magnetic field energized by an exothermic chemical reaction administered by Arrhenius kinetics," *Int. J. Heat Mass Transf.*, vol. 129, pp. 198–211, 2019, doi: 10.1016/j.ijheatmasstransfer.2018.09.105.

[16] O. D. Makinde, "Exothermic explosions in a slab: A case study of series summation technique," *Int. Commun. Heat Mass Transf.*, vol. 31, no. 8, pp. 1227–1231, 2004, doi: 10.1016/j.icheatmasstransfer.2004.08.020.

[17] S. O. Salawu, R. A. Kareem, M. D. Shamshuddin, and S. U. Khan, "Double exothermic reaction of viscous dissipative Oldroyd 8-constant fluid and thermal ignition in a channel," *Chem. Phys. Lett.*, vol. 760, no. 138011, p. 138011, 2020, doi: 10.1016/j.cplett.2020.138011.

[18] S. O. Adesanya, J. A. Falade, S. Jangili, and O. Anwar Bég, "Irreversibility analysis for reactive third-grade fluid flow and heat transfer with convective wall cooling," *Alex. Eng. J.*, vol. 56, no. 1, pp. 153–160, 2017, doi: 10.1016/j.aej.2016.09.017.

[19] A. Starikovskiy and N. Aleksandrov, "Plasma-assisted ignition and combustion," *Prog. Energy Combust. Sci.*, vol. 39, no. 1, pp. 61–110, 2013, doi: 10.1016/j.pecs.2012.05.003.

[20] A. Osamura, H. Horisawa, and T. Sakai, "Characteristics of a laser-electrostatic hybrid propulsion thruster," in *50th AIAA/ASME/SAE/ASEE Joint Propulsion Conference*, Reston, Virginia: American Institute of Aeronautics and Astronautics, 2014.

[21] J. Gao *et al.*, "The free radical mechanism of electromagnetic field affecting explosion of premixed methane," *Combust. Flame*, vol. 234, no. 111649, p. 111649, 2021, doi: 10.1016/j.combustflame.2021.111649.

[22] S. Kinoshita, T. Takagi, H. Kotera, and N. I. Wakayama, "Numerical simulation of diffusion flames with and without magnetic field," *IEEE Trans. Appl. Supercond.*, vol. 14, no. 2, pp. 1685–1688, 2004, doi: 10.1109/tasc.2004.831035.

[23] D. Glushkov, K. Paushkina, and A. Pleshko, "Gel fuels: Preparing, rheology, atomization, combustion," *Energies*, vol. 16, no. 1, p. 298, 2022, doi: 10.3390/en16010298.

[24] M. B. Padwal, B. Natan, and D. P. Mishra, "Gel propellants," *Prog. Energy Combust. Sci.*, vol. 83, no. 100885, p. 100885, 2021, doi: 10.1016/j.pecs.2020.100885.

[25] R. Arnold, P. H. S. Santos, O. H. Campanella, and W. E. Anderson, "Rheological and thermal behavior of gelled hydrocarbon fuels," *J. Propuls. Power*, vol. 27, no. 1, pp. 151–161, 2011, doi: 10.2514/1.48936.

[26] D. Galecki, "Ignition and combustion of metallized propellants," in *25th Joint Propulsion Conference*, Reston, Virigina: American Institute of Aeronautics and Astronautics, 1989.

[27] S. Rahimi, A. Peretz, and B. Natan, "On shear rheology of gel propellants," *Propellants Explos. Pyrotech.*, vol. 32, no. 2, pp. 165–174, 2007, doi: 10.1002/prep.200700018.

[28] G. Li, M. Zhang, H. Ji, Y. Ma, T. Chen, and L. Xie, "The optimization of Carreau model and rheological behavior of alumina/linear low-density polyethylene composites with different alumina content and diameter," *E-polymers*, vol. 21, no. 1, pp. 742–753, 2021, doi: 10.1515/epoly-2021-0077.

[29] U. Ghosh, "Electro-magneto-hydrodynamics of non-linear viscoelastic fluids," *J. Nonnewton. Fluid Mech.*, vol. 277, no. 104234, p. 104234, 2020, doi: 10.1016/j.jnnfm.2020.104234.

[30] S. Salawu and A. Okedoye, "Thermodynamic second law analysis of hydromagnetic gravity-driven two-step exothermic chemical reactive flow with heat absorption along a channel," *Iranica Journal of Energy & Environment*, vol. 9, no. 2, pp. 114–120, 2018.

[31] S. O. Salawu, M. S. Dada, and O. J. Fenuga, "Thermal explosion and irreversibility of hydromagnetic reactive couple stress fluid with viscous dissipation

and Navier slips," *Theor. Appl. Mech. Lett.*, vol. 9, no. 4, pp. 246–253, 2019, doi: 10.1016/j.taml.2019.04.003.

[32] O. D. Makinde and O. A. Bég, "On inherent irreversibility in a reactive hydromagnetic channel flow," *J. Therm. Sci.*, vol. 19, no. 1, pp. 72–79, 2010, doi: 10.1007/s11630-010-0072-y.

[33] P. K. Pattnaik, S. R. Mishra, O. Anwar Bég, U. F. Khan, and J. C. Umavathi, "Axisymmetric radiative titanium dioxide magnetic nanofluid flow on a stretching cylinder with homogeneous/heterogeneous reactions in Darcy-Forchheimer porous media: Intelligent nanocoating simulation," *Mater. Sci. Eng. B Solid State Mater. Adv. Technol.*, vol. 277, no. 115589, p. 115589, 2022, doi: 10.1016/j.mseb.2021.115589.

[34] E. Sozer, "Multiscale porous media modelling for liquid rocket injector application," in *42nd AIAA/ASME/SAE/ASEE Joint Propulsion Conference & Exhibit 9*, Sacramento, California, 2006.

[35] U. A. Jeigarnik, F. P. Ivanov, and N. P. Ikranikov, "Experimental data on heat transfer and hydraulic resistance in unregulated porous structures," *Teploenergetika*, no. 2, pp. 33–38, 1991.

[36] J. Lux, D. Suslov, and O. Haidn, "Experimental investigation of porous injectors for liquid propellant rocket engines," in *44th AIAA/ASME/SAE/ASEE Joint Propulsion Conference & Exhibit*, Reston, Virigina: American Institute of Aeronautics and Astronautics, 2008.

[37] S. Whitaker, "The Forchheimer equation: A theoretical development," *Transp. Porous Media*, vol. 25, no. 1, pp. 27–61, 1996, doi: 10.1007/bf00141261.

[38] A. E. Scheidegger, "The physics of flow through porous media," *Soil Sci.*, vol. 86, no. 6, p. 355, 1958, doi: 10.1097/00010694-195812000-00015.

[39] O. A. Bég and O. D. Makinde, "Viscoelastic flow and species transfer in a Darcian high-permeability channel," *J. Pet. Sci. Eng.*, vol. 76, no. 3–4, pp. 93–99, 2011, doi: 10.1016/j.petrol.2011.01.008.

[40] J. C. Umavathi and O. Anwar Bég, "Numerical study of double-diffusive dissipative reactive convective flow in an open vertical duct containing a non-Darcy porous medium with Robin boundary conditions," *J. Eng. Math.*, vol. 119, no. 1, pp. 135–147, 2019, doi: 10.1007/s10665-019-10022-w.

[41] M. Nasir, M. Waqas, O. A. Bég, and N. Zamri, "Homotopy analysis of mixed convection flow of a magnetized viscoelastic nanofluid from a stretching surface in

non-Darcy porous media with revised Fourier and Fickian approaches," *Waves Random Complex Media*, pp. 1–28, 2023, doi: 10.1080/17455030.2023.2178824.

[42] S. Rawat, R. Bhargava, R. Bhargava, and O. A. Bég, "Transient magneto-micropolar free convection heat and mass transfer through a non-Darcy porous medium channel with variable thermal conductivity and heat source effects," *Proc Inst Mech Eng Part C*, vol. 223, no. 10, pp. 2341–2355, 2009, doi: 10.1243/09544062jmes1483.

[43] C. Geindreau, "Auriault Magnetohydrodynamic flows in porous media," *J. Fluid Mech*, vol. 466, pp. 343–363, 2002.

[44] J. Mcwhirter, M. Crawford, and D. Klein, "Magnetohydrodynamic flows in porous media II: Experimental results," *Fusion Technol*, vol. 34, pp. 187–197, 1988.

[45] K. A. Yih, "The effect of uniform suction/blowing on heat transfer of magnetohydrodynamic Hiemenz flow through porous media," *Acta Mech.*, vol. 130, no. 3–4, pp. 147–158, 1998, doi: 10.1007/bf01184307.

[46] S. K. Ghosh, O. Bég, R. Bhargava, S. Rawat, and T. A. Bég, "Mathematical modelling of transient magnetohydrodynamic couple stress fluid flow in a rotating channel," *Int. J. Applied Mathematics and Mechanics*, vol. 6, no. 6, pp. 23–45, 2010.

[47] J. Zueco, O. A. Beg, and L. M. L. Ochoa, "Non-linear transient hydromagnetic partially ionised dissipative Couette flow in a non-Darcian porous medium channel with Hall, ionslip and Joule heating effects," *Prog. Comput. Fluid Dyn.*, vol. 11, no. 2, p. 116, 2011, doi: 10.1504/pcfd.2011.038837.

[48] K. Maqbool, O. Anwar Bég, A. Sohail, and S. Idreesa, "Analytical solutions for wall slip effects on magnetohydrodynamic oscillatory rotating plate and channel flows in porous media using a fractional Burgers viscoelastic model," *Eur. Phys. J. Plus*, vol. 131, no. 5, 2016, doi: 10.1140/epjp/i2016-16140-5.

[49] A. Castellanos, Ed., *Electrohydrodynamics*. Vienna, Austria: Springer, 1998.

[50] V. K. Narla, D. Tripathi, D. S. Bhandari, and O. A. Bég, "Electrokinetic insect bioinspired membrane pumping in a high aspect ratio bio microfluidic system," *Microfluidics and Nanofluidics*, 2022.

[51] O. A. Bég, M. Hameed, and T. A. Bég, "Chebyschev spectral collocation simulation of nonlinear boundary value problems in electrohydrodynamics," *Int. J. Computational Methods in Engineering Science and Mechanics*, vol. 14, pp. 104–115, 2013, doi: 10.1080/15502287.2012.698707

[52] D. Tripathi, A. Yadav, and O. Anwar Bég, "Electro-osmotic flow of couple stress fluids in a micro-channel propagated by peristalsis," *Eur. Phys. J. Plus*, vol. 132, no. 4, 2017, doi: 10.1140/epjp/i2017-11416-x.

[53] P. O. Bedolla, G. Vorlaufer, P. Sequard-Base, A. Vernes, and F. Franek, "Altitude dependence of electrohydrodynamic flow in an electrostatic lifter," *J. Electrostat.*, vol. 87, pp. 32–44, 2017, doi: 10.1016/j.elstat.2017.03.003.

[54] O. A. Bég, T. A. Bég, S. R. Munjam, and S. Jangili, "Homotopy and adomian semi-numerical solutions for oscillatory flow of partially ionized dielectric hydrogen gas in a rotating MHD energy generator duct," *Int. J. Hydrogen Energy*, vol. 46, no. 34, pp. 17677–17696, 2021, doi: 10.1016/j.ijhydene.2021.02.189.

[55] V. H. Granados, M. J. Pinheiro, and P. A. Sá, "Electrostatic propulsion device for aerodynamics applications," *Phys. Plasmas*, vol. 23, no. 7, p. 073514, 2016, doi: 10.1063/1.4958815.

[56] J. P. Boeuf, Y. Lagmich, T. Unfer, T. Callegari, and L. C. Pitchford, "Electrohydrodynamic force in dielectric barrier discharge plasma actuators," *J. Phys. D Appl. Phys.*, vol. 40, no. 3, pp. 652–662, 2007, doi: 10.1088/0022-3727/40/3/s03

[57] J. A. del Río and S. Whitaker, *Transp. Porous Media*, vol. 44, no. 2, pp. 385–405, 2001, doi: 10.1023/a:1010762226382.

[58] J. L. Auriault and T. Strzelecki, "On the electro-osmotic flow in a saturated porous media," *Int. J. Engng Sci*, vol. 19, pp. 915–928, 1981.

[59] M. M. Bhatti, A. Zeeshan, N. Ijaz, O. Bég, and A. Kadir, "Mathematical modelling of nonlinear thermal radiation effects on EMHD peristaltic pumping of viscoelastic dusty fluid through a porous medium channel," *Engineering Science and Technology*, vol. 20, no. 3, pp. 1129–1139, 2017, doi: 10.1016/j.jestch.2016.11.003

[60] C. Vargas, J. Arcos, O. Bautista, and F. Mendez, "Hydrodynamic dispersion in a combined magnetohydrodynamic-electroosmotic-driven flow through a microchannel with slowly varying wall zeta potentials," *Phys. Fluids*, vol. 29, 2017, doi: 10.1063/1.4991680

[61] Y. Jian and L. Chang, "Electromagnetohydrodynamic (EMHD) micropumps under a spatially non-uniform magnetic field," *AIP Adv.*, vol. 5, no. 5, p. 057121, 2015, doi: 10.1063/1.4921085.

[62] D. Si and Y. Jian, "Electromagnetohydrodynamic (EMHD) micropump of Jeffrey fluids through two parallel microchannels with corrugated walls," *J. Phys. D Appl. Phys.*, vol. 48, no. 8, p. 085501, 2015, doi: 10.1088/0022-3727/48/8/085501.

[62] D. Tripathi, A. Sharma, and O. Anwar Bég, "Joule heating and buoyancy effects in electro-osmotic peristaltic transport of aqueous nanofluids through a microchannel with complex wave propagation," *Adv. Powder Technol.*, vol. 29, no. 3, pp. 639–653, 2018, doi: 10.1016/j.apt.2017.12.009.

[63] R. Chakraborty, R. Dey, and S. Chakraborty, "Thermal characteristics of electromagnetohy-drodynamic flows in narrow channels with viscous dissipation and Joule heating under constant wall heat flux," *Int. J. Heat Mass Transf*, vol. 67, pp. 1151–1162, 2013, doi: 10.1016/j.ijheatmasstransfer.2013.08.099.

[64] L. Zhang, M. M. Bhatti, O. A. Bég, H. J. Leonard, and S. Kuharat, "Numerical study of natural convection dissipative electro-magnetic non-Newtonian flow through a non-Darcy channel," *Z. Angew. Math. Mech.*, vol. 102, no. 10, 2022, doi: 10.1002/zamm.202100608.

[65] M. T. Mollah, "EMHD laminar flow of Bingham fluid between two parallel Riga plates," *Heat Technol.*, vol. 37, no. 2, pp. 641–648, 2019, doi: 10.18280/ijht.370236.

[66] J. C. Umavathi and O. A. Bég, "Double-diffusive convection in a dissipative electrically conducting nanofluid under orthogonal electric and magnetic fields: A numerical study," *Nanosci. Technol. Int. J.*, vol. 12, no. 2, pp. 59–90, 2021, DOI: 10.1615/NanoSciTechnolIntJ.2021036786

[67] C. Yoon, S. D. Heister, G. Xia, and C. L. Merkle, "Numerical modeling of injection of shear-thinning gel propellants through plain-orifice atomizer," *J. Propuls. Power*, vol. 27, no. 5, pp. 944–954, 2011, doi: 10.2514/1.b34135.

[68] P. J. Carreau, "Rheological equations from molecular network theories," *Trans. Soc. Rheol.*, vol. 16, no. 1, pp. 99–127, 1972, doi: 10.1122/1.549276.

[69] S. S. Okoya, "On criticality and disappearance of criticality for a branched-chain thermal reaction with distributed temperature," *Afr. Mat.*, vol. 24, no. 4, pp. 465–476, 2013, doi: 10.1007/s13370-012-0070-1.

[70] M. R. Osborne, "On shooting methods for boundary value problems," *J. Math. Anal. Appl.*, vol. 27, no. 2, pp. 417–433, 1969, doi: 10.1016/0022-247x(69)90059-6.

[71] G. Adomian, *Solving frontier problems of physics: The decomposition method*, 1994th ed. Dordrecht, Netherlands: Springer, 2013.

[72] Y. Cherruault, "Convergence of Adomian's method," *Kybernetes*, vol. 18, no. 2, pp. 31–38, 1989, doi: 10.1108/eb005812.

[73] O. A. Bég, D. Tripathi, T. Sochiand, and P. K. Gupta, "Adomian decomposition method (ADM) simulation of magneto-biotribological squeeze film with magnetic

induction effects," *J. Mechanics Medicine Biology*, vol. 15, 2015, doi: 10.1142/S0219519415500724

[74] M. Shamshuddin, S. R. Mishra, A. Bég, and A. Kadir, "Adomian computation of radiative-convective stretching flow of a magnetic non-Newtonian fluid in a porous medium with homogeneous-heterogeneous reactions," *Int. J Modern Phy. B*, vol. 33, no. 2, 2020.

[75] A. K. Al-Hadhrami, L. Elliott, D. B. Ingham, "A new model for viscous dissipation in porous media across a range of permeability values," *Transp. Porous Media, vol. 53, pp. 117–122, 2003,* doi: 10.1023/A:1023557332542.

[78] J. D. Seader, W. J. Rivers, and R. J. Ingram, "Effect of porosity zoning and matrix material on the performance of self-cooled nozzle throat inserts," *J. Spacecr. Rockets*, vol. 3, no. 7, pp. 1138–1140, 1966, doi: 10.2514/3.28614.

[79] M. S. Z. Norouzi, Anwar Bég, "Exact analysis of heat convection of viscoelastic FENE-P fluids through isothermal slits and tubes," *Meccanica*, vol. 53, pp. 817–831, 2018, doi: 10.1007/s11012-017-0782-2

[80] F. T. Akyildiz and K. Vajravelu, "Magnetohydrodynamic flow of a viscoelastic fluid," *Phys. Lett. A*, vol. 372, no. 19, pp. 3380–3384, 2008, doi: 10.1016/j.physleta.2008.01.073.

[81] S. Das, R. R. Patra, and R. N. Jana, "Hydromagnetic oscillatory reactive flow through a porous channel in a rotating frame subject to convective heat exchange under Arrhenius kinetics," *J. Eng. Phys. Thermophys.*, vol. 94, no. 3, pp. 702–713, 2021.

[82] S. Das, N. Mahato, A. Ali, and R. N. Jana, "Aspects of Arrhenius kinetics and Hall currents on gyratory Couette flow of magnetized ethylene glycol containing bi-hybridized nanomaterials," *Heat Trans*, vol. 52, no. 4, pp. 2995–3026, 2023.

APPENDIX 1 : ADOMIAN DECOMPOSITION METHOD (ADM)

ADM [71, 73, 74] is quantitative rather than qualitative and furthermore is rigorously analytic, requiring neither linearization nor perturbation. It is a *continuous solution methodology* and circumvents the need with other techniques for discretization (e. g. the finite element method) and consequent computer-intensive calculations. A further advantage of ADM is that since highest ordered derivative are easily invertible operators, laborious integrations involving complicated Green functions, can be avoided. Consider a general differential equation with V as the variable, of the form:

$$D[V(y)] = Q(y) \tag{A1}$$

Here, D is the differential operator consists of linear terms $(L+R)$ with L being the highest ordered derivative and easily invertible operator and R is the Adomian reminder linear component and $Nu(y)$ is the Adomian nonlinear component. Each of the transformed governing equations for momentum and energy i. e. Eqns. (14)-(15) feature two dependent variables (u, T) and one independent variable (y). For example, the momentum Eqn. (14) can be written as:

$$Lu(y) + Ru(y) + Nu(y) = Q(y) \tag{A2}$$

Now the solution $u(y)$ is obtained by solving the Eqn. (A2) for $Lu(y)$. Since the n^{th} order L is the highest ordered derivative and easily invertible, then L^{-1} Is the $n-$fold integral operator. Thus, Eqn. (A2) can be written as:

$$u(y) = L^{-1}Q(y) - L^{-1}Ru(y) - L^{-1}Nu(y) \tag{A3}$$

Next, we introduce L_1 & L_2 as the 3rd and 2nd order differential operators, $L_1 = \frac{d^3}{dy^3}(*)$ and $L_2 = \frac{d^2}{dy^2}(*)$ respectively. Consequently, L_1^{-1} & L_2^{-1} are the $3-$fold & $2-$fold indefinite integral operators, $L_1^{-1}(*) = \int_0^y \int_0^y \int_0^y (*) dydydy$ and $L_2^{-1}(*) = \int_0^y \int_0^y (*)\, dydy$ respectively. Furthermore, the constants of integration in L_1^{-1} & L_2^{-1} are computed from the given initial and boundary conditions. ADM assumes the solution *u(y)* as an infinite series:

$$u(y) = \sum_{y=0}^{\infty} u_n \tag{A4}$$

which is the unknown solution for the velocity field, *u(y).* Similarly, for temperature, the Adomian series solutions take the form:

$$T(y) = \sum_{y=0}^{\infty} T_n(y) \tag{A5}$$

Finally, the non-linear term $Nu(y)$ assumed to analytic and by writing as an infinite series, we have for the velocity field:

$$Nu(y) = \sum_{y=0}^{\infty} A_n \tag{A6}$$

Here A_n represents the Adomian polynomials which are lengthy expressions and are omitted for brevity. Further details are provided in Adomian [**71**].